

MEASUREMENT OF NEUTRON SPECTRA  
FOLLOWING STOPPED MUON CAPTURE  
ON LIQUID DEUTERIUM

by

André Spence Turcot  
B.Sc., Concordia University, Montréal, P.Q., 1985

A THESIS SUBMITTED IN PARTIAL FULFILLMENT  
OF THE REQUIREMENTS FOR THE DEGREE OF  
MASTER OF SCIENCE  
in the Department  
of  
Physics

ACCEPTED  
FACULTY OF GRADUATE STUDIES

We accept this dissertation as conforming  
to the required standard

October 6, 1987

DEAN

Supervisor Dr. G.R. Mason

Dr. L.P. Robertson

Dr. C. S. Wu

Dr. V.K. Bhargava

Dr. A. Fry

©ANDRÉ S. TURCOT, 1987  
UNIVERSITY OF VICTORIA






*All rights reserved. This dissertation may not be reproduced  
in whole or in part, by xerography or other means,  
without the permission of the author.*

### Abstract

Supervisor: Professor G. R. Mason

The energetic neutron spectrum following stopped muon capture on liquid deuterium has been measured for the first time. The measurement, performed at TRIUMF, used a high purity liquid deuterium target. The energy measurement was based on the time-of-flight technique which relied on detecting both neutrons present in the final state within a constrained geometry. The final spectrum obtained shows evidence of a possible enhancement of the neutron yield in the 35-50 Mev energy range. The findings are consistent with the prediction for the high energy neutron limit of a 200% enhancement due to meson exchange currents. The results show that further experimental investigation of light nuclei ( $A \leq 4$ ) is necessary to determine whether meson exchange currents are responsible for the observed enhancements in the energetic particle spectrum following muon capture in heavier nuclei.

Examiners:

  
\_\_\_\_\_  
Dr. G.R. Mason  
  
\_\_\_\_\_  
Dr. L.P. Robertson  
  
\_\_\_\_\_  
Dr. C.S. Wu  
  
\_\_\_\_\_  
Dr. V.K. Bhargava  
  
\_\_\_\_\_  
Dr. A. Fry

# Contents

Abstract . . . . .	ii
Table of Contents . . . . .	iii
List of Figures . . . . .	v
Acknowledgement . . . . .	viii
<b>1 Introduction</b>	<b>1</b>
<b>2 Muon Capture on Deuterium</b>	<b>6</b>
2.1 Experimental Aspects . . . . .	7
2.1.1 Muon Catalyzed Fusion . . . . .	8
2.1.2 Previous Measurements of the Capture Rate . . . . .	10
2.2 Theoretical Aspects of $\mu^-$ Capture . . . . .	12
2.2.1 Current-Current Weak Hamiltonian . . . . .	12
2.2.2 Impulse Approximation and Meson Exchange Currents	17
2.2.3 Elementary Particle Method . . . . .	19
<b>3 The Experiment</b>	<b>25</b>
3.1 Experimental Apparatus and Technique . . . . .	27
3.1.1 TRIUMF M20A Channel . . . . .	30
3.1.2 Liquid Deuterium Target . . . . .	30
3.1.3 Neutron Detection System . . . . .	32
3.1.4 Muon Telescope and Veto System . . . . .	34
3.2 Electronics and Timing . . . . .	37
<b>4 Analysis of Data and Results</b>	<b>44</b>

4.1	Analysis Technique . . . . .	45
4.1.1	Calibration of TOF TDC Spectra . . . . .	45
4.1.2	Calibration of ADC Spectra . . . . .	47
4.1.3	Analysis Leading to the Energy Spectrum . . . . .	50
4.1.4	Discussion of the Background . . . . .	58
4.1.5	Neutron Energy Spectrum . . . . .	63
<b>5</b>	<b>Extensions of the Experiment</b>	<b>65</b>
5.1	An Improved Technique for Deuterium . . . . .	66
5.1.1	Pulse Shape Discrimination . . . . .	67
5.1.2	Neutron Detection System . . . . .	68
5.2	Measurement of the Neutron Spectra for $^3\text{He}$ . . . . .	72
5.2.1	Experimental Technique for $^3\text{He}$ . . . . .	74
<b>6</b>	<b>Conclusion</b>	<b>78</b>
	<b>References</b>	<b>80</b>

# List of Figures

2.1	Theoretical energetic neutron spectrum, based on EPM calculation; the effect of the inclusion of the meson exchange correction term is shown for the case that it applies over a 15 Mev energy range. . . . .	23
2.2	Differential capture rate for: a) Mirror form factor b) Analytic continuation c,d,e) MEC Enhancement extrapolated over 14, 10, 6 Mev neutron energy ranges, respectively. . . .	24
3.1	Dalitz plot of available phase space for final state. Contours represent fixed values of $\theta_{nn}$ . . . . .	27
3.2	Relationship of neutron energies for fixed time delays between Near and Far Counter signals. . . . .	28
3.3	Experimental arrangement in target area showing muon telescope, veto system and neutron counters, only three of the twelve Far counters are shown for clarity. . . . .	29
3.4	TRIUMF M20 channel, the channel divides into M20A and M20B at bending magnet M20B2. . . . .	31
3.5	Target Assembly showing liquid deuterium target cell, designed by Caffrey <i>et al.</i> . . . . .	33
3.6	2 $\mu$ sec TDC for all runs, the scale factor from channel number to ns approximately is 1 to 1. Note that time goes from right to left. . . . .	36

3.7	Muon Telescope and Veto System, FI refers to a fan-in and led to a leading edge discriminator. . . . .	37
3.8	2 $\mu$ sec TDC and pile up circuits. . . . .	38
3.9	Master Gate (MG). . . . .	38
3.10	Back to Back requirement, the logic is detailed for Far counter 10 and Near counter 1 or 2. . . . .	39
3.11	Timing at input to Master Gate and TDC's . . . . .	40
3.12	Simplified experimental schematic showing the logic at the input to the Master Gate and TOF TDC's. . . . .	41
3.13	Arrangement of neutron counters showing $16^\circ$ angular requirement. . . . .	42
4.1	Timing resolution obtained from $\pi^-$ data. . . . .	46
4.2	Time-of-flight vs. 2 $\mu$ sec TDC, axes expressed in arbitrary units. . . . .	49
4.3	Energy resolution, kinematic and finite counter thickness effects. The 1.1 ns timing resolution is superimposed as boxes. . . . .	50
4.4	Neutron detection efficiencies, output of GRACE. . . . .	52
4.5	Time-of-flight vs. amplitude of Far counters, arbitrary units. . . . .	53
4.6	Time-of-flight vs. amplitude of Near counters, arbitrary units. . . . .	53
4.7	Finite target volume effect, coincidence efficiency as a function of position along target axis for different neutron energies. . . . .	55
4.8	Integrated coincidence efficiency for various stopping profiles. . . . .	57
4.9	Raw time-of-flight spectrum used to obtain final energy spectrum showing background level. . . . .	58
4.10	Raw time-of-flight spectrum showing background level. . . . .	60
4.11	Raw time-of-flight spectrum showing background level. . . . .	61
4.12	Neutron Spectrum, See text for description. . . . .	63
5.1	Coincidence efficiency for $\Delta\theta < 26^\circ$ . Compare with Fig. 4.7. . . . .	69

5.2	Proposed counter arrangement showing the angular acceptance for new latch pattern. . . . .	70
5.3	Time-of-flight spectrum for $\Delta\theta < 16^\circ$ . The 22 to 33 ns interval has 368 counts with a background of 261. . . . .	71
5.4	Time-of-flight spectrum for $\Delta\theta < 26^\circ$ . The 22 to 33 ns interval has 752 counts with a background of 500. . . . .	72

## Acknowledgement

I would like to thank my supervisor, Dr. Gren Mason, for making it possible to continue my education in physics through his support. I also wish to extend thanks for his suggestions and guidance regarding this thesis.

As well, I would like to acknowledge the work by other members of the group who performed the experiment: Drs. T.J. Hallman, L. Madansky, S. Trentalange, E.K. McIntyre and T.R. King. In particular, Dr. Yung Keun Lee, the group spokesman and whose comments and advice regarding the analysis were indispensable. I would also like to express thanks to A.J. Caffrey who wrote the initial version of the analysis programme.

I am also indebted to Dr. S. Beingessner, with whom many ideas regarding this thesis were discussed and for the ensuing suggestions. I would like to thank Dr. P. Poffenberger for helpful discussions regarding the experimental aspects of the thesis.

Finally, I would like to thank Julia MacCartney for her proof reading and my dear Natasha, who drew the circuit diagrams.

# Chapter 1

## Introduction

Nuclear muon capture is a manifestation of the weak interaction. It provides an excellent means of testing our knowledge of the weak force. The most common weak process is the decay of the neutron. The interaction most akin to muon capture is electron or K-capture, a form of  $\beta$  decay. The electron and muon differ only in mass and the phenomenological assignment of lepton number. The much greater muon mass ( $\approx 207m_e$ ) manifests itself in the following manner: a matrix element describing a semi-leptonic nuclear interaction can be thought of as the image of the nucleus while being viewed with the wavelength corresponding to the lepton momentum. For negative muon,  $\mu^-$ , capture, as opposed to  $\beta$  decay, the associated neutrino momentum is much greater; thus, the nucleus is probed on a finer scale. The probability of a given final state is dependent on the matrix element, which in turn is dependent on the form factors describing the distribution of the weak currents responsible for the transition. The form factors are functions of  $q^2$ , the momentum transfer. In  $\beta$  decay  $q^2$  is practically zero, whereas in  $\mu^-$  capture, the functional dependence of the form factors can be investigated over a range of values.

The first stage of the nuclear capture process, atomic capture of the muon, is well understood [1]. A  $\mu^-$  passing through matter first loses energy via ionization. Once the energy of the muon is comparable to the orbital

kinetic energy for a given quantum state it is captured by the Coulomb field of the nucleus. The atomic capture occurs in an orbit corresponding to a large value of  $n$ , the principle quantum number that defines the size of the atomic orbital according to

$$r(n) = \frac{\hbar^2 n^2}{m_{red} e^2 Z} \quad (1.1)$$

where  $m_{red}$  is the reduced mass of the muon nucleus system and  $Z$  is the atomic number of the nucleus. The inner muonic orbits lie well within the electron K-shell; thus, the muonic atom is effectively a two body system.<sup>1</sup> The lower energy muonic orbits are unoccupied; thus, the  $\mu^-$  will quickly cascade electromagnetically down to the 1S orbit by Auger (emission of an orbital electron) and radiative transitions. The time taken for the atomic capture and cascade process is negligible compared to the muon lifetime.

The initial distribution of the 1S hyperfine states is assumed to be statistical. The muon will remain in the 1S orbital until it either decays according to:



or interacts with a proton in the nucleus according to the fundamental capture reaction:



The decay rate,  $\lambda_0 = 4.55 \times 10^5 \text{ sec}^{-1}$ , is much greater than the nuclear capture rate for light nuclei. The capture rate is approximately equal to the decay rate for  $Z \approx 12$  and is roughly proportional to  $Z^4$  [2]. The fundamental capture process is well understood within the framework of the V–A weak interaction theory. Work performed in the past fifteen years at meson “factories” has solidified our understanding of the muonic aspects of

---

<sup>1</sup>There is a small effect due to the finite probability that an orbital electrons may be found within the muon orbit.

the weak interaction. Experiments have shown us that the muon and electron interact with matter with the same coupling constants and have led to the hypothesis of electron-muon universality. Muon capture experiments on hydrogen have vindicated the V–A form of the weak interaction and provided limits for the weak coupling constants. For light nuclei,  $Z \leq 12$ , the measured capture rates are within fair agreement (10%) with the theoretical predictions; interestingly, capture processes dominated by the axial vector component of the weak interaction have theoretical values *consistently* lower than experiment, though not in disagreement. By trying to explain these differences, a better understanding of nuclear structure may be obtained.

The motivation for studying deuterium comes from recent work in the study of energetic particle emission following muon capture on heavier nuclei. Previously, in a TRIUMF experiment, the observation of a large enhancement in the energetic components of the neutron spectra of  $^{165}\text{Ho}$  was reported [3]. Bernabéu *et al.*[4], for the case of medium heavy nuclei, predict a lower bound of 1 to 2% of energetic neutron emission corresponding to an energy transfer of roughly 80% or more of the muon rest mass to the emitted particles. They have suggested on the basis of such enhancements that the similarity between  $\pi^-$  capture and the high energy component of  $\mu^-$  capture may be fundamental in nature.

For the case of deuterium, a 200% enhancement of the capture rate has been predicted [5] for the limiting case of zero neutrino momentum. This corresponds to maximum energy transfer to the nucleons in the final state. The predicted enhancement in the extreme time-like region of momentum transfer<sup>2</sup> is due to meson exchange currents which arise from the effects of inter-nucleon binding and are described to first order by the inter-nucleon exchange of pions. The magnitude of the axial vector coupling is

---

<sup>2</sup>The time-like region of momentum transfer is  $0 < q^2 \leq m_\mu^2$  where  $m_\mu$  is the muon rest mass. The extreme time-like region is where  $q^2 \approx m_\mu^2$ .

related to pionic processes and the capture process in deuterium is dominated by the axial vector term. As well, the time-like region contributes 25% of the total capture rate. Consequently, it is evident that muon capture on deuterium is an excellent candidate for detection of axial current related effects on energetic particle emission.

A measurement of the neutron spectrum would help delineate theoretical techniques of determining the capture rate by providing an additional constraint besides agreement with the total capture rate. Calculations to determine the capture rate,  $\Lambda_c$ , require integration of the theoretically derived neutron spectrum. Until now no portion of the spectrum had been experimentally measured to provide a guide to these calculations. The recent measurement of the doublet capture rate [6] disagrees with calculations based on the impulse approximation with inclusion of meson exchange effects[8,9]; an observed enhancement in the energetic portion of the neutron spectrum would help to determine the nature of the discrepancy.

The purpose of TRIUMF experiment 297 [7] was to investigate the high energy neutron spectrum from stopped muon capture on deuterium with the goal of detecting the predicted renormalization of the capture rate due to meson exchange currents. The experiment was also the first attempt to measure any portion of the neutron spectrum. The experiment is part of a study investigating energetic particle emission after nuclear  $\mu^-$  capture. In this thesis, the measurement and subsequent analysis is detailed. By utilizing a novel time-of-flight detection system, the neutron spectrum in the 25 to 50 Mev region has been successfully measured for the first time. The results are not inconsistent with the assumption of an enhancement based on meson exchange corrections in the extreme high energy (time-like) region.

The following topics will be dealt with in this thesis: Chapter 2 deals with the required theoretical framework to study muon capture and selected applications to deuterium; as well the results of previous experimental ef-

forts with deuterium are presented along with a brief discussion of the effects of muon induced chemistry in hydrogen isotopes; in Chapter 3 the experimental technique is outlined with emphasis on the time-of-flight system and in Chapter 4 the analysis of the data and the results are presented. Chapter 5 considers the proposed extensions of the experiment to  $^3\text{He}$  and  $^4\text{He}$ , as well as methods of improving upon the present measurement for deuterium.

## Chapter 2

# Muon Capture on Deuterium

Muon capture on deuterium is the simplest example of nuclear capture by a composite nucleus. The process has only one basic reaction channel:



The capture process is an almost pure Gamow-Teller transition due to the effect of the Pauli Exclusion Principle on the final state. Experimental study of the capture process on deuterium provides an excellent opportunity to test theoretical models for many aspects of nuclear physics. Two body nuclear potentials may be tested as well as our basic understanding of the weak interaction involving multiple hadronic systems. Meson exchange currents (MEC) account for the observed discrepancy in low energy deuteron production and photo-disintegration of the deuteron at higher energies [10]. The extension of MEC effects to weak processes based on the techniques employed in electromagnetic processes requires experimental verification [8]. The capture process for deuterium is the only experimental test for the two-body weak exchange current operators. By measuring the capture rate and neutron spectrum, the nuclear weak current is probed and the effects of nucleon-nucleon coupling can be measured.

## 2.1 Experimental Aspects

From an experimentalist's viewpoint, the study of  $\mu^-$  capture on deuterium is fraught with difficulties. The capture process competes with muon decay and meso-molecular processes that induce nuclear fusion. The decay rate is three orders of magnitude larger than the total capture rate. All particles in the final state are electrically neutral; hence particle detection is difficult. The cross section for transfer of a  $\mu^-$  to an atom of greater  $Z$  is large:



the transfer rate being of the order of  $10^{11} \text{ s}^{-1}$ . This implies that the sample must be kept ultra-pure. The nuclear capture reaction has a very strong hyperfine dependence. For deuterium, the capture rate from the doublet hyperfine state is approximately 60 times that of the quartet capture rate [13] and the transition rates between the hyperfine states are not precisely known. In a pure liquid  $\text{D}_2$  target, a large low energy neutron flux is produced by muon catalyzed fusion. For experiments based on neutron detection, the fusion neutron background can be prohibitive.

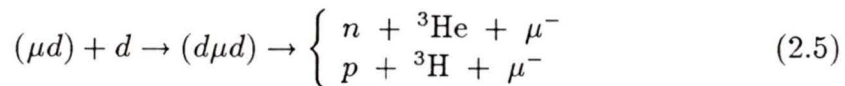
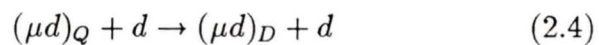
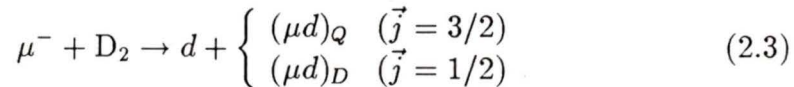
It was because of the above reasons that almost all previous work has focussed on determination of the capture rate. It is only now that the spectrum measurement has been attempted. The main reasons why the measurement was previously thought nigh impossible was the lack of a proper means to measure the neutron energy and the prohibitive background. The standard technique of neutron energy determination over a wide range of possible values is the time-of-flight technique. In complex nuclei, the capture process is usually accompanied by simultaneous emission of discrete  $\gamma$  rays associated with transitions in the residual nucleus. The gamma ray can provide a time-zero signal for the time-of-flight measurement. The problem with deuterium is the lack of a proper time-zero signal;

there are no  $\gamma$  rays associated with the basic capture process<sup>1</sup> and the lifetime of the muon in the target is too long for the muon stop signal to supply an accurate time-zero signal. This problem has been circumvented in the present measurement by implementation of a novel time-of-flight system.

### 2.1.1 Muon Catalyzed Fusion

When a negative muon is stopped in a target containing deuterium, a complex sequence of events is initiated, which has a high probability of culminating in  $\mu^-$  catalyzed fusion. After the fusion process, the muon may be liberated to re-enter the cycle. The catalysis cycle is very complex and a detailed description of the formation mechanisms for hydrogen mesomolecules is beyond the scope of this thesis, though the salient features pertinent to  $\mu^-$  capture will be outlined.

The cycle begins with capture of the muon by a deuterium molecule and subsequent molecular disassociation.



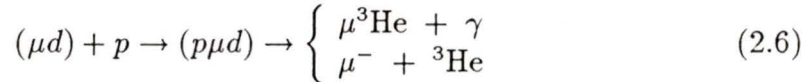
The muonic atom is formed with a statistical population of quartet and doublet hyperfine states, reaction 2.3, and with a kinetic energy greater than the thermal energy of the target. Once the  $\mu d$  atom is thermalized, inelastic scattering produces an irreversible spinflip transition, reaction 2.4. The energetically favourable quartet to doublet transition quickly depopulates the quartet state.<sup>2</sup> The average lifetime of the quartet state in a liquid  $D_2$  target,  $t_{mean} \approx 23$  ns [17], is fast on the muon time scale. This implies

<sup>1</sup>Neglecting radiative muon capture

<sup>2</sup>The doublet state is more tightly bound by 0.15 eV.

that a measurement of the capture rate is predominately the doublet state capture rate. The formation of the  $d\mu d$  meso-molecule, reaction 2.5, has a large hyperfine dependence on the state of the  $\mu d$  atom. The ratio of the  $d\mu d$  formation rate from the quartet state to that from the doublet state is approximately 80. Once in the  $d\mu d$  state, fusion is almost instantaneous, occurring at a rate of about  $10^9 \text{ s}^{-1}$ . The branching ratio for the  $n+{}^3\text{He}$  channel is  $0.55 \pm .05$  [15]. The fate of the muon after fusion is dependent on the “sticking” fraction  $\omega$ ; which is the probability that the muon will remain bound to the fusion products. For  ${}^3\text{He}$  produced in reaction 2.5, the sticking probability,  $\omega_{He}^{dd}$ , is  $0.126 \pm .004$  [18]. For the other fusion channel,  $\omega_H \approx 0.01$  is negligible. In all, about 94% of the muons are free to reenter the cycle.

Even in an ultra-pure target there is still some protium contamination; this enables formation of the  $p\mu d$  meso-molecule. The proton and deuteron undergo fusion;



but at a much smaller rate, about  $10^5 \text{ s}^{-1}$ [15]. For the first channel of reaction 2.6, the sticking fraction is large,  $\omega_{He}^{pd} = 0.84 \pm 0.04$  [18]; the muon has a high probability of being removed from the catalysis cycle and possibly interacting with the helium nucleus. From the above figures, it can be shown that in a liquid  $\text{D}_2$  target that after one  $\mu\text{s}$  the muon has spent 97% of the time in the  $(\mu d)_{1/2}^S$  state and 3% bound to  ${}^3\text{He}$  [6]. The capture rate for  ${}^3\text{He}$  is five times that for deuterium; thus, it can be a source of background. The quantitative effects of this on the present measurement will be discussed in Chapter 4.

### 2.1.2 Previous Measurements of the Capture Rate

The first attempts at measuring the capture rate,  $\Lambda_c$ , were performed by a Columbia University group [15] and by a Bologna-CERN collaboration [16]. Both employed the “classical” method of measuring  $\Lambda_c$ , a technique based on the observation of the neutrons produced by the capture reaction. The deuterium capture energy spectrum is peaked at 1.5 Mev and the neutrons have a maximum energy of approximately 51 Mev. Neutrons from  $d\mu d$  fusion,  $E_{fus} = 2.44$  Mev, overlap the spectrum and can be an overwhelming source of background. In an attempt to control the  $d\mu d$  fusion background, both experiments employed deuterated hydrogen (protium) targets. The transfer rate for  $\mu p$  to  $\mu d$  is very fast on the muon lifetime scale, being of the order of  $10^9$  s<sup>-1</sup>. The reduced deuterium concentration ensured that the production of  $d\mu d$  would be minimal.

The Columbia group employed a liquid hydrogen target with a deuterium concentration of 0.32%. The liquid state of the target implied that the formation of  $p\mu d$  molecules, which also undergo fusion, was not negligible. The fusion product, <sup>3</sup>He, has a large probability of having the  $\mu^-$  remain bound, thus producing a neutron background from capture on <sup>3</sup>He.<sup>3</sup> The capture process took place predominately in the  $p\mu d$  molecule. Because of this, the muon may also be captured by the proton nucleus. The culmative effect of this is that the observed neutrons were a sum of three possible captures: on protons, deuterons and <sup>3</sup>He. The time distribution of the emitted neutrons was analyzed and a figure of 30% was calculated to be the contribution from capture on deuterium.<sup>4</sup> The published result for the deuterium capture rate was  $365 \pm 96$  s<sup>-1</sup>. The quoted error would be very difficult to improve upon considering the limitations of the technique.

The Bologna-CERN group used a gaseous hydrogen target at 7.6 at-

---

<sup>3</sup>The <sup>3</sup>He capture process will be detailed in Chapter 5.

<sup>4</sup>Neutrons from capture on <sup>3</sup>He and protons will have different transient spectra. The time spectra were inferred from previous capture studies on <sup>3</sup>He and protons.

mospheres and 293 K with a 5% admixture of deuterium. The measurement was a major improvement over the Columbia experiment. The decreased density of the target limited the  $p\mu d$  formation; thus, the neutrons were primarily from capture on deuterium. The published result was  $445 \pm 60 \text{ s}^{-1}$ . This was interpreted to be the doublet capture rate and is in agreement with theoretical predictions [8,9,13].

The fact that the state of the  $\mu d$  atom at the time of capture is difficult to assess has raised controversy over the experimental results obtained for the capture rate. Breunlich [19] had argued that the published results are in error for the Columbia and Bologna-CERN experiments. Breunlich believes that the assumption of pure doublet state occupation for the Bologna-CERN experiment is not correct; he argues that capture was from a statistical sampling of hyperfine states via consideration of the target conditions and the known meso-molecular reaction rates. He calculates a corrected value for the doublet capture rate to be  $970 \pm 130 \text{ s}^{-1}$ . For the Columbia experiment, where a statistical distribution was originally assumed, reanalysis by Breunlich yielded a value of  $210 \pm 60 \text{ s}^{-1}$ . Since these results are in obvious conflict, the experiment was repeated using a different technique.

The latest measurement performed by a Saclay-CERN-Bologna group [6] used the lifetime technique. The technique is based on comparison of the lifetimes of positive and negative muons stopped in the target. This was the first measurement to employ an ultra-pure liquid deuterium target. A stopped muon signal opened a  $65 \mu\text{s}$  gate during which a system of 6 particle telescopes monitored the target for the mu-decay electron. The correction for capture on  $^3\text{He}$  was computed by two independent methods and the correction for the muon lifetime due to the atomic binding (about  $12 \text{ s}^{-1}$ ) was also taken into account. The final result published was  $470 \pm 29 \text{ s}^{-1}$ . The result was shown to be the doublet state capture rate from analysis based

on the latest values for the relevant meso-molecular processes. This value is in agreement with the previous CERN-Bologna result but at odds with theoretical predictions using the impulse approximation with the inclusion of meson exchange terms [8,9,11]. From this analysis, we may conclude that in the present measurement, where the target conditions were nearly identical, the capture process was exclusively from the doublet state.

## 2.2 Theoretical Aspects of $\mu^-$ Capture

This section will deal with the theoretical framework on which  $\mu^-$  capture is based. The basic V–A structure of the weak process will be reviewed (see for example Mukhopadhyay [1]). The Effective Hamiltonian [14] for muon capture will be presented as well as the relevant results from two techniques of calculating capture rates: the Nucleon Only Impulse Approximation (NOIA) and the Elementary Particle Method (EPM) as applied to deuterium. The effect of meson exchange currents (MEC) will be presented within the context of the present measurement.

### 2.2.1 Current-Current Weak Hamiltonian

Nuclear muon capture is based on a four fermion current-current interaction. The original form of which is due to Fermi [21], who patterned the weak interaction on the electromagnetic one. Lee and Yang [24] extended Fermi's theory to include the observed parity violation in weak interactions [25]. With the Conserved Vector Current theory of Feynman and Gell-Mann [26], the present V–A form of the weak interaction was attained.

The form of the Hamiltonian,  $\mathcal{H}_\mu$ , for the fundamental capture reaction,  $\mu^- + p \rightarrow n + \nu_\mu$ , may be arrived at under very general constraints. Starting from the standard four fermion form of the V–A interaction and invoking Lorentz covariance and the Gell-Mann Cabbibo universality [23],

one arrives at

$$\mathcal{H}_\mu = \frac{G \cos \theta_c}{\sqrt{2}} (V_\lambda^\dagger + A_\lambda^\dagger) L_\lambda + \text{h.c.} \quad (2.7)$$

where  $G$  is the Fermi coupling constant,  $\theta_c$  is the Cabbibo angle and h.c. denotes the hermitian conjugate. This is the strangeness preserving ( $\Delta S = 0$ ), singly charged ( $\Delta Q = \pm 1$ ), isovector ( $|\Delta I| = 1$ ) semi-leptonic weak Hamiltonian density. The hadronic vector and axial vector matrix elements may be phenomenologically obtained as (see for example Sakurai [22]), respectively:

$$V_\lambda^\dagger = \bar{\psi}_n (g_V \gamma_\lambda - (\frac{g_M}{2M}) \sigma_{\lambda\rho} q_\rho - (i \frac{g_S}{m_\mu} q_\lambda)) \psi_p \quad (2.8)$$

$$A_\lambda^\dagger = \bar{\psi}_n (g_A \gamma_\lambda \gamma_5 - (\frac{g_T}{2M}) \sigma_{\lambda\rho} q_\rho \gamma_5 - (i \frac{g_P}{m_\mu} q_\lambda \gamma_5)) \psi_p \quad (2.9)$$

The lepton matrix element has pure V–A structure

$$L_\lambda = \bar{\psi}_\nu \gamma_\lambda (1 + \gamma_5) \psi_\mu \quad (2.10)$$

where the  $\gamma_\lambda$ 's are the 4x4 Dirac gamma matrices which satisfy the following relations:

$$[\gamma_\lambda, \gamma_\rho]_+ = 2\delta_{\lambda\rho}, \quad [\gamma_\lambda, \gamma_\rho] = -2i\sigma_{\lambda\rho}, \quad \gamma_5 = \gamma_1 \gamma_2 \gamma_3 \gamma_4 \quad (2.11)$$

The  $\psi_\alpha$ 's are four component fermion spinors, where the overhead bar signifies the adjoint,  $\psi^\dagger \gamma_4$ . The  $(1 + \gamma_5)$  term acts as a projector for left-handed lepton states, giving parity violation.  $M$  and  $m_\mu$  are the nucleon and muon masses respectively. The form factors  $g_i$  are functions of  $q^2$ , where  $q_\rho = n_\rho - p_\rho$  is the momentum transfer at the interaction vertex. The form factors describe the distribution of the weak currents and their names arise from the behaviour of the associated combination of  $\gamma$  matrices under a Lorentz transformation;  $g_V \gamma_\lambda \equiv$  vector,  $g_P \gamma_5 \equiv$  pseudoscalar, etc. The exception is  $g_M$ , the weak magnetic form factor which transforms as a proper tensor.

The form factors  $g_M, g_P, g_S, g_T$  are induced by the strong interactions of the hadrons. The currents may be further classified according to the behaviour under G-parity.<sup>5</sup> If the requirement that all the respective members of the axial and vector hadronic currents exhibit the same behaviour under the G-parity transformation, then the scalar and tensor form factors  $g_S, g_T$  are set to zero because the strong interaction is invariant under G-parity. Weinberg [28] termed these currents “second class” because of their irregular behaviour under the G-parity transformation. If the demand that  $\mathcal{H}_\mu$  be invariant under time reversal, T, then all the form factors are real, implying as well that CP is conserved.

### CVC and PCAC Hypotheses

The Conserved Vector Current (CVC) hypothesis relates the electromagnetic and vector weak currents. The CVC states that the isovector component of the nuclear electromagnetic current,  $\frac{1}{2}\psi\gamma_\lambda\tau_z\psi$ , and the weak currents  $V_\lambda, V_\lambda^\dagger$  form an isovector. The CVC implies that since the electromagnetic current is conserved<sup>6</sup> and the coupling constant is unaffected by the meson cloud; the same applies to the vector components of the weak current. Thus, the bare vector coupling constants used in pure leptonic weak processes are unaffected by the strong interaction. Furthermore, in the low energy limit as  $q^2 \rightarrow 0$ , the CVC relates the vector and weak magnetic form factors to the electromagnetic form factors obtained from electron scattering off nucleons. In terms of the Dirac and Pauli form factors, ( $q^2$  dependence suppressed) this is expressed as [1];

$$g_V(q^2) = g_{Dirac}^p - g_{Dirac}^n, \quad g_V(0) = 1 \quad (2.12)$$

$$g_M(q^2) = g_{Pauli}^p - g_{Pauli}^n, \quad g_M(0) = (\mu_p - \mu_n) \quad (2.13)$$

<sup>5</sup>G-parity is defined as  $G = Ce^{i\pi\tau_y}$  where  $\tau_y$  is the appropriate isospin operator for the multiplet and C is the charge conjugation operator. G-parity induces a rotation of  $180^\circ$  about the y-axis of “charge space” and changes the sign of the charge.

<sup>6</sup>The contribution from meson currents must be taken into account.

where  $\mu_p, \mu_n$  are the anomalous magnetic moments of the proton and neutron respectively. The CVC also predicts that the scalar form factor  $g_S$  equals zero as each member of the vector current must be divergenceless, *i.e.* conserved.

The PCAC (Partial Conservation of Axial Current) states that the axial current, an isovector, is partially conserved. The divergence of  $A_\lambda$  is proportional to a pseudoscalar which is interpreted to be the pion field. If the axial current were conserved, the decay of a pion to a muon would be forbidden. The axial components of the weak current are renormalized by the strong interaction. The value of  $g_A(q^2 = 0) = 1.254 \pm 0.007$  is obtained from the free neutron  $\beta$ -decay rate <sup>7</sup> [29]. The  $q^2$  dependence is found via pion production from neutrino scattering off protons and deuterons and is found to satisfy a dipole fit [1]. The induced pseudoscalar form factor,  $g_P$ , is not readily measurable. It is obtained from the assumption that in a semi-leptonic interaction, the pion-pole dominates the contribution to  $g_P$ . The contribution may be expressed as [32]

$$g_P(q^2) = \frac{-\sqrt{2} m_\pi f(-m_\pi^2) g_{\pi N}}{q^2 + m_\pi^2} \quad (2.14)$$

where  $f(-m_\pi^2)$  is related to pion decay and  $g_{\pi N}$  is the pion-nucleon coupling constant. With the further assumption that the divergence of  $A_\lambda$  is also dominated by the pion-pole for small  $q^2$ , one obtains the Goldberger-Trieman relationship [33] and is able to then relate  $g_P$  to  $g_A(0)$ :

$$g_P(q^2) = \frac{2M g_A(0)}{q^2 + m_\pi^2} \quad (2.15)$$

If the strong force was “turned off” and hadrons were point-like, then the induced form factors would vanish and the vector and axial vector couplings

---

<sup>7</sup>A value of  $|g_A/g_V| = 1.24$  at  $q^2 = 0$  can be obtained from field theoretic considerations that relate pion-nucleon cross sections in an analogous manner to the derivation of the vector form factors using the CVC [30,31].

would be equal.

### Primakoff Effective Hamiltonian

Primakoff and Fujii [14], in an effort to extend the theory of muon capture to composite nuclei, derived a general Hamiltonian for the process. For a nucleus of  $Z$  protons and  $A-Z$  neutrons, the Hamiltonian is given in a configuration space representation as

$$H_{eff} = \frac{1}{\sqrt{2}} \tau^{(+)} \frac{(1 - \boldsymbol{\sigma} \cdot \boldsymbol{\nu}_1)}{\sqrt{2}} \sum_{i=1}^A \tau_i^{(-)} (G_V \mathbf{I} \cdot \mathbf{I}_i + G_A \boldsymbol{\sigma} \cdot \boldsymbol{\sigma}_i - G_P \boldsymbol{\sigma} \cdot \boldsymbol{\nu}_1 \boldsymbol{\sigma}_i \cdot \boldsymbol{\nu}_1) \delta(\vec{r} - \vec{r}_i) \quad (2.16)$$

where the “effective” vector, axial vector and induced pseudo-scalar couplings are respectively given as:

$$G_V \equiv g_V \left(1 + \frac{\nu}{2m_p}\right) \quad (2.17)$$

$$G_A \equiv g_A - g_V (1 + \mu_p - \mu_n) \frac{\nu}{2m_p} \quad (2.18)$$

$$G_P \equiv [g_P - g_A - g_V (1 + \mu_p - \mu_n)] \frac{\nu}{2m_p} \quad (2.19)$$

and  $\boldsymbol{\nu} = \nu \boldsymbol{\nu}_1$  is the neutrino momentum;  $\mathbf{I}$ ,  $\mathbf{I}_i$  and  $\boldsymbol{\sigma}$ ,  $\boldsymbol{\sigma}_i$  are  $2 \times 2$  unit matrix and spin operators for the lepton and  $i$ th nucleon;  $\vec{r}$  and  $\vec{r}_i$  are the space coordinates of the lepton and  $i$ th nucleon; the  $\tau^{(+)}$  and  $\tau_i^{(-)}$  are isospin operators which transform the muon into a mu-neutrino and the  $i$ th proton into a neutron; the  $(1 - \boldsymbol{\sigma} \cdot \boldsymbol{\nu}_1)$  term produces parity violation.

The Hamiltonian was derived with a non-relativistic treatment of the nucleons and muon, though all terms of the order of  $\nu/m_p$  were kept. Inherent in the derivation is the assumption of V-A structure, the CVC, absence of second class currents and time reversal invariance. There are no terms corresponding to meson exchange processes.

The “effective” couplings or form factors may be grouped according to the nature of the transition. The Fermi and Gamow-Teller transition form factors are expressible as:

$$\Gamma_F = G_V^2; \quad \Delta \vec{J} = 0 \quad (2.20)$$

$$\Gamma_{GT} = 3G_A^2 + (G_P^2 - 2G_A^2 G_P^2); \quad \Delta \vec{J} = 0 \pm 1, \quad \text{no } 0 \rightarrow 0 \quad (2.21)$$

### 2.2.2 Impulse Approximation and Meson Exchange Currents

One approach for dealing with complex nuclei is the Nucleons Only Impulse Approximation (NOIA). The basis of this approximation is that the weak properties of the nucleons are identical to the properties of free neutrons and protons. The effective weak nuclear current is the sum of the individual nucleon currents with appropriate phases taken into consideration. The total momentum transferred in the interaction is absorbed by one nucleon without subsequent exchange of mesons. In reality, the nuclear weak current has contributions from nuclear iso-bars and mesons. For the case of capture on deuterium, the largest correction to the effective Hamiltonian, equation 2.16, is due to the process

$$\mu^- + p'(i)n(i) \rightarrow \nu_\mu + \Delta' + n(i) \rightarrow \nu_\mu + n'(f) + \pi^0 + n(i) \rightarrow \nu_\mu + n'(f) + n(f) \quad (2.22)$$

where (i) and (f) refer to the initial and final states of the nucleons and  $\Delta'$  is a nucleon iso-bar. The prime on the initial proton is used to distinguish the particles. The meson exchange corrections are represented by a sum of terms, each depending on the spin, iso-spin and inter-nucleon distance of the nucleon pairs. The NOIA technique has been applied to deuterium [34,35]; the more recent calculation of Dautry *et al.* [8] and the analysis of Goulard *et al.* [5] for capture in the extreme time-like region will be the focus of this section.

Dautry *et al.* applied the Primakoff Effective Hamiltonian and considered the effect of meson exchange currents on the doublet capture rate. They observed that the primary nuclear transition is from the  ${}^3S_1$  deuteron state to the  ${}^1S_0$  n-n state. This is a Gamow-Teller transition and is dominated by the axial vector coupling. To gauge the effects of the MEC correction to the overall capture rate, they considered only the contribution to the axial vector term.<sup>8</sup> To simplify the calculation, they also only considered the MEC correction applied to transitions leading to the  ${}^1S_0$  final state. The effect was computed with the inclusion of the deuteron S and D states. Using the Reid Soft-Core potential [36] for the final state, the capture rates obtained were  $\Lambda_D^{Imp} = 381 \text{ s}^{-1}$  for the doublet state and  $\Lambda_Q^{Imp} = 13 \text{ s}^{-1}$  for the quartet state. The correction for MEC terms to the doublet state was found to be  $\delta\Lambda_D = 24 \text{ s}^{-1}$ , yielding a total rate of  $\Lambda_D = 405 \text{ s}^{-1}$ . The MEC correction has been calculated elsewhere [11] using the hard pion approach and was stated to be  $32.4 \text{ s}^{-1}$ . Refined calculations of the doublet capture rate do not vary greatly amongst each other. Without the inclusion of MEC terms, the average value obtained is  $381 \text{ s}^{-1}$ .

Goulard *et al.* considered the MEC effects on the capture process in the limiting case of zero neutrino momentum. They obtained an expression which included MEC corrections that was valid for any value of neutrino momentum; thus, in principle, applicable to any possible final state over the entire range of neutron energies. To ensure the consistency of the approach, they first compared their expression for the capture rate to that of Dautry *et al.* by restricting the sum over final states to the  ${}^1,{}^3S_0$  component.<sup>9</sup> The limiting case of zero neutrino momentum was then considered. The previously required infinite summation of neutrino partial waves is reduced to two terms, restricting the allowed final states. The allowed n-n final

<sup>8</sup>Recall that in the limit  $q^2 \rightarrow 0$ , the CVC predicts that the vector current is unaffected.

<sup>9</sup>The notation for states is  ${}^{2S+1,2T+1}L_J$ .

states are  $^1,^3S_0$ ,  $^3,^3P_0$ ,  $^3,^3P_1$ ,  $^1,^3D_2$ , and  $[^3,^3P_2 - ^3,^3F_2]$ , where the brackets indicate coupled waves. In this limit, the capture rate may be expressed as:

$$\frac{d\Lambda}{dE_n} = \left[ \frac{2G \cos \theta_c}{\pi} \right]^2 |\phi_\mu(\vec{r}=0)|^2 F(E_n) \times \Sigma \quad (2.23)$$

where

$$\Sigma = |b_{1111}^0(\vec{\nu}=0)|^2 + \frac{1}{3} \Sigma_{LSJ} |b_{0LSJ}^1(\vec{\nu}=0)|^2, \quad J \leq 2 \quad (2.24)$$

where  $\phi_\mu$  is the muon 1S state function,  $F(E_n)$  is derived from the kinematic constraints and  $b_{1111}^0$  and  $b_{0LSJ}^1$  correspond, respectively, to the time and space parts of the nuclear transition operator. The quantity  $\Sigma$  is then evaluated considering only the NOIA contribution and then the NOIA plus MEC contribution. The effect of the meson exchange currents is expressed in terms of X, where X is defined as

$$X = \frac{\Sigma(\text{NOIA} + \text{MEC}) - \Sigma(\text{NOIA})}{\Sigma(\text{NOIA})} \quad (2.25)$$

When all final n-n states are taken into account, the value of X is 2; in other words, the capture rate is enhanced by 200% by the MEC terms. The  $^1,^3D_2$  and the  $^1,^3S_0$  continuum partial waves are the predominant final states. Comparison of the MEC effect for the kinematic region of low neutrino momentum to that of high neutrino momentum, where the majority of capture takes place [8], shows that the MEC effect is much greater (a factor of approximately 30) in the high neutron energy, low neutrino momentum limit.

### 2.2.3 Elementary Particle Method

The Elementary Particle Method (EPM) is based on treating the initial and final nuclear states as elementary particles of the appropriate spin

and parity. In principle, any nuclear sub-structure is absorbed into the form factors. The advantages of the EPM are that the treatment is fully relativistic and nuclear wave functions are not required; thus, nuclear potential model dependence is eliminated. The disadvantage is that analysis of multi-particle final states is difficult.

Mintz [13], in a series of calculations, has applied the EPM technique to the case of capture on deuterium. The calculation was performed without recourse to an impulse based calculation of the axial vector form factor. He fitted data from the pion photo-production reaction,  $\gamma + d \rightarrow n + n + \pi^+$ , to the derived PCAC result for this reactions form factors. The matrix elements for pion-photoproduction are then related to those for  $\mu^- + d \rightarrow n + n + \nu_\mu$ . It is pointed out that the approach, *in principle*, contains all Feynman diagrams to first order in G, implying that at least some MEC effects are included despite the required approximations. It should be stressed that the form of  $F_A(q^2)$ <sup>10</sup> is obtained only in the space-like region,  $m_\mu^2 \leq q^2 \leq 0$ ; *an assumption must be made regarding the behaviour in the time-like region,  $0 \geq q^2 \geq m_\mu^2$* . The vector form factors for reaction 2.1 were arrived at using data from deuteron photo and electro-disintegration and the CVC.

The total capture rate obtained assuming a statistical population of the hyperfine 1S states was  $\Lambda = 155 \text{ s}^{-1}$ , the doublet capture rate,  $\Lambda_D$ , was  $450.4 \text{ s}^{-1}$  and the quartet rate,  $\Lambda_Q$ , was  $7.3 \text{ s}^{-1}$ . The doublet rate is in excellent agreement with the two latest experimental results. Mintz stresses that the capture rate is dominated by the axial vector term,  $F_A$ , and the time-like region contributes one quarter of the total rate. Mintz then explores the effect of varying the behaviour of the axial form factor in the time-like region on the capture rate. He considers three assumptions for the functional dependence of  $F_A(q^2)$ :

<sup>10</sup>The convention for the form factor nomenclature is that of the original papers [13], in terms of the notation of eq. 2.9, this would correspond to  $g_A(q^2)$ .

1. the form factor is analytically continued from the space-like to time-like regions
2. (i,ii) the time-like form factor is functionally identical to the space-like term but  $q^2 \rightarrow -q^2$ ;

$$F_A(q^2) \approx F_A(q'^2), \quad q'^2 = -q^2 \quad (2.26)$$

Part of the axial current form factor in the space-like region is the dipole fit:

$$F_A(q^2) = \frac{F_A(0)}{\left(1 - \frac{q^2}{M_A^2}\right)^2}, \quad M_A = 912 \text{ Mev} \quad (2.27)$$

where  $M_A$  was determined from analysis of pion photo-production data. Because of the multi-particle final state,  $F_A(q^2)$  is not completely defined by just  $q^2$ ; it also depends on the relative neutron and deuteron momenta.<sup>11</sup> With regard to equation 2.26, the assumption can be considered to apply to (i) the complete  $F_A(q^2)$  or (ii) only to the dipole term of the form factor in the space-like region.

The three assumptions were tested and no discernable difference on the total capture rate was observed,  $\Delta\Lambda < 1 \text{ s}^{-1}$ . Comparison of the differential capture rates (neutron spectra) for the three assumptions; however, showed a 10% enhancement in the 35 to 50 Mev neutron range for the analytic continuation of  $F_A(q^2)$  compared to the two other assumptions (mirror form factors). The results based on the assumptions of equation 2.26 exhibited a difference of no more 0.3% in the time-like region. This led Mintz to propose that measurements over the entire neutron spectrum be performed to determine whether the analytic continuation is an acceptable *ansatz*.

The theoretical spectrum is shown in figure 2.1, it corresponds to the analytic continuation; on this scale the 10% difference between the

---

<sup>11</sup>The complete functional dependence of the form factor is not required to illustrate the point in question and will not be presented.

assumptions for  $F_A(q^2)$  does not manifest itself. The small enhancement extending from 35 Mev to 51 Mev corresponds to inclusion of meson exchange currents. Although the original calculation of the enhancement [5] only strictly applies to the kinematic limit of zero neutrino momentum, the 200% enhancement has been extrapolated over the last 15 Mev of the neutron spectrum. The extrapolation was performed assuming a linear, monotonically decreasing effect over the energy range. Strictly speaking, the enhancement should be applied to a spectrum based on an NOIA calculation, but this was unavailable. The form of the extrapolation is an assumption required by the fact that at present there is no calculation available describing MEC effects over the whole energy spectrum including all final states. The spectra obtained by assuming different extrapolation ranges is shown in Fig. 2.2; on this scale the difference between the analytic continuation and mirror form factor are apparent.

Year	Exp. $s^{-1}$	Theo. $s^{-1}$	Ref.
1965	$365 \pm 96$		[15]
1965		334	[34]
1972		313	[35]
1973	$445 \pm 60$		[16]
1976		405	[8]
1979		413	[12]
1980		450	[13]
1985	$470 \pm 29$		[6]

Table 2.1: Previous values obtained for the doublet capture rate

The present theoretical situation regarding muon capture on deuterium requires clarification. The recent measurement of the doublet capture rate does not agree with predictions based on the impulse approximation. The inconsistency can be somewhat lessened by including corrections due to MEC effects on the dominant partial waves. The prediction based on the elementary particle technique, although in good agreement with ex-

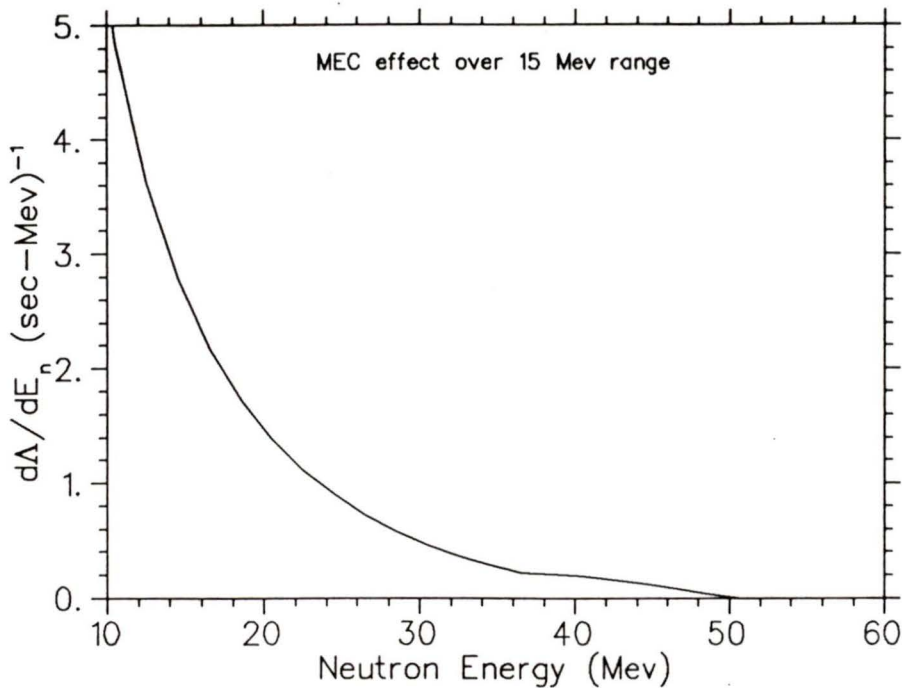


Figure 2.1: Theoretical energetic neutron spectrum, based on EPM calculation; the effect of the inclusion of the meson exchange correction term is shown for the case that it applies over a 15 MeV energy range.

periment, suffers from the necessity of assuming the functional dependence of the axial current form factor, which as previously stated, is the dominant contributor to the transition operator describing the capture process in deuterium. It should also be pointed out that muon capture on nuclei (D,  $^3\text{He}$ ,  $^6\text{Li}$ ) that are predominately axial vector induced captures have theoretical values slightly lower than experiment<sup>12</sup>[1]; the discrepancy is most evident in the case of deuterium. It is not unreasonable that experimental measurement of neutron spectrum for deuterium might give insight in the nature of the discrepancy and point out possible shortcomings of the impulse approximation.

<sup>12</sup>The theoretical values are consistently near the lower limit of the experimental uncertainty.

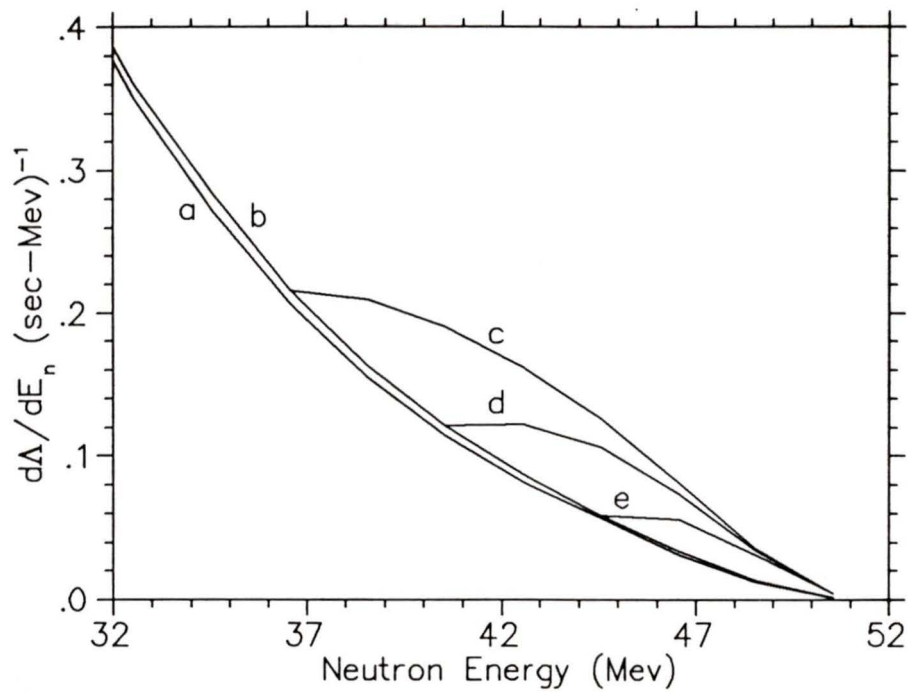


Figure 2.2: Differential capture rate for: a) Mirror form factor b) Analytic continuation c,d,e) MEC Enhancement extrapolated over 14, 10, 6 Mev neutron energy ranges, respectively.

# Chapter 3

## The Experiment

TRIUMF experiment 297<sup>1</sup> was the first attempt to measure the neutron spectrum from  $\mu^-$  capture on deuterium and was designed to measure neutrons in the 25 to 50 Mev energy range. The experiment exploited the fact that in the kinematic region of interest, the two neutrons are emitted in a nearly back-to-back configuration with similar energies. For fast neutrons,  $E \geq 3$  Mev, the standard technique of energy measurement is by time-of-flight (TOF). The time difference between signals from detectors a known distance apart may be used to compute the particle's velocity. The problem with applying this technique to deuterium is the lack of a proper time-zero or start signal. In order to overcome this problem, the TOF system devised for this experiment was novel; *both emitted neutrons* were required to be detected in order to compute the time-of-flight. This requirement also served as the primary means to reduce the background.

### Back-to-Back Requirement and Kinematic Effects

The neutron detection system had to be able to measure the neutron's energy accurately and be able to discriminate events attributable to the capture process. The final state of the capture process,  $\mu^- + d \rightarrow n + n + \nu_\mu$ , is characterized by two neutrons and a muon neutrino. The neutrino is

---

<sup>1</sup>The group spokesman was Professor Y.K. Lee of the Johns Hopkins University.

essentially undetectable due to its weak interaction with matter. To bias the detection system for events attributable to a deuteron capture event, both neutrons were required to be detected within a  $\pm 16^\circ$  deviation from a pure back-to-back geometry.

The final state neutron energies are related according to the following expression:<sup>2</sup>

$$\begin{aligned} & \left[ \left( \frac{Q - E_1 + m_n}{p_1} \right)^2 - \cos^2 \theta_{nn} \right] E_2^2 \\ - 2 & \left[ \frac{\left( \frac{Q^2}{2} - E_1(Q + m_n) \right) (Q - E_1 + m_n)}{p_1^2} + m_n \cos^2 \theta_{nn} \right] E_2 \\ & + \left( \frac{Q^2}{2} - E_1(Q + m_n) \right)^2 \frac{1}{p_1} = 0 \end{aligned} \quad (3.1)$$

where  $Q$  is the available kinetic energy (102.1 Mev) from the capture reaction;  $m_n$  is the neutron rest mass;  $E_1$  and  $E_2$  are the respective neutron kinetic energies;  $p_1$  is the neutron momentum and  $\theta_{nn}$  is the angle between their momenta.

The motivation for the back-to-back requirement comes from the kinematics for 25-50 Mev capture neutrons. Consider a Dalitz plot, Fig. 3.1, showing the available phase space in the center-of-momentum system for the three-body final state. The contours show the neutron energy dependence for fixed angles between the directions of the emitted neutrons. It can be seen that for 25 Mev neutrons, the minimum angle is approximately  $165^\circ$ . Consider, now, a superimposed family of curves representing fixed time delays between a time-zero signal from a counter near to the target and a stop signal from a detector placed on the other side of the target. This is shown in Fig. 3.2 for the case where the counter distances are 25 cm and 244 cm, respectively. It can be seen that, for a given time difference, the energy of the neutron detected in the Far counter is almost

<sup>2</sup>The equation was derived using relativistic kinematics with no approximations.

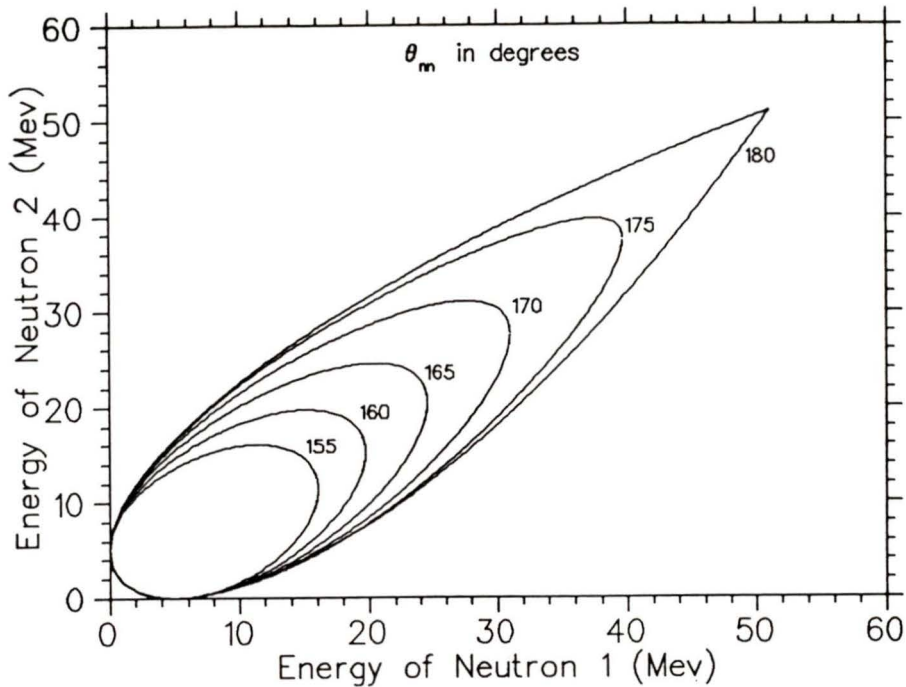


Figure 3.1: Dalitz plot of available phase space for final state. Contours represent fixed values of  $\theta_{nm}$ .

independent of the energy of the neutron triggering the Near counter. The variation in the neutron time-of-flight from the target to the Near counters implies that there is a kinematic effect on the energy resolution. This effect will be further discussed in Chapter 4.

### 3.1 Experimental Apparatus and Technique

The experimental target area is shown in Fig. 3.3. Eight counters, placed at approximately 25 cm from the target, were used for the time-zero signals and twelve counters, placed at 244 cm from the target, supplied the stop signals. The Far counters were viewed from both top and bottom with photomultiplier tubes employed in a mean time mode. The energy of neutron triggering the Far counter was calculated from the time difference between the time-zero signal and the average time of the two Far counter

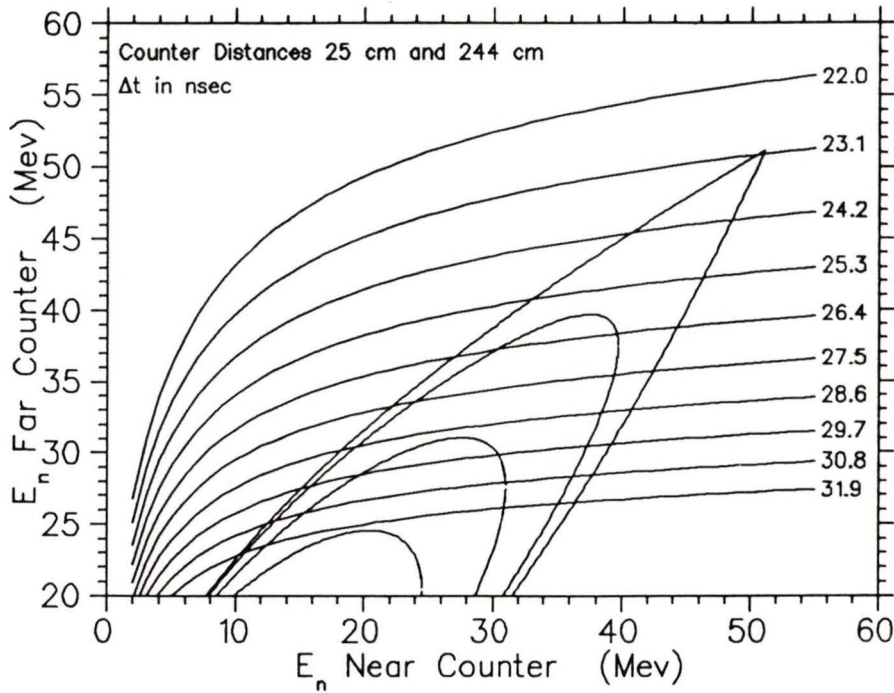


Figure 3.2: Relationship of neutron energies for fixed time delays between Near and Far Counter signals.

signals. The flight path used for calculating the velocity, hence energy, was obtained by subtracting the distance from the target to the Near counters from the distance from the target to the Far counters.

Particles entering the target area, ( $\mu^-$ ,  $\pi^-$ ,  $e^-$ ), were detected by use of a particle telescope. To shield the neutron counters from charged particles emanating from the target area, a double layer of charged particle detectors were used as vetos. The  $\mu^-$  stopping rate in the central region of the high purity 440 cm<sup>3</sup> liquid D<sub>2</sub> target was maximized by an electron telescope. The data acquisition system was based on a PDP 11/34 computer interfaced via a CAMAC system to the detector electronics; data were recorded on magnetic tapes in the TRIUMF MULTI format.

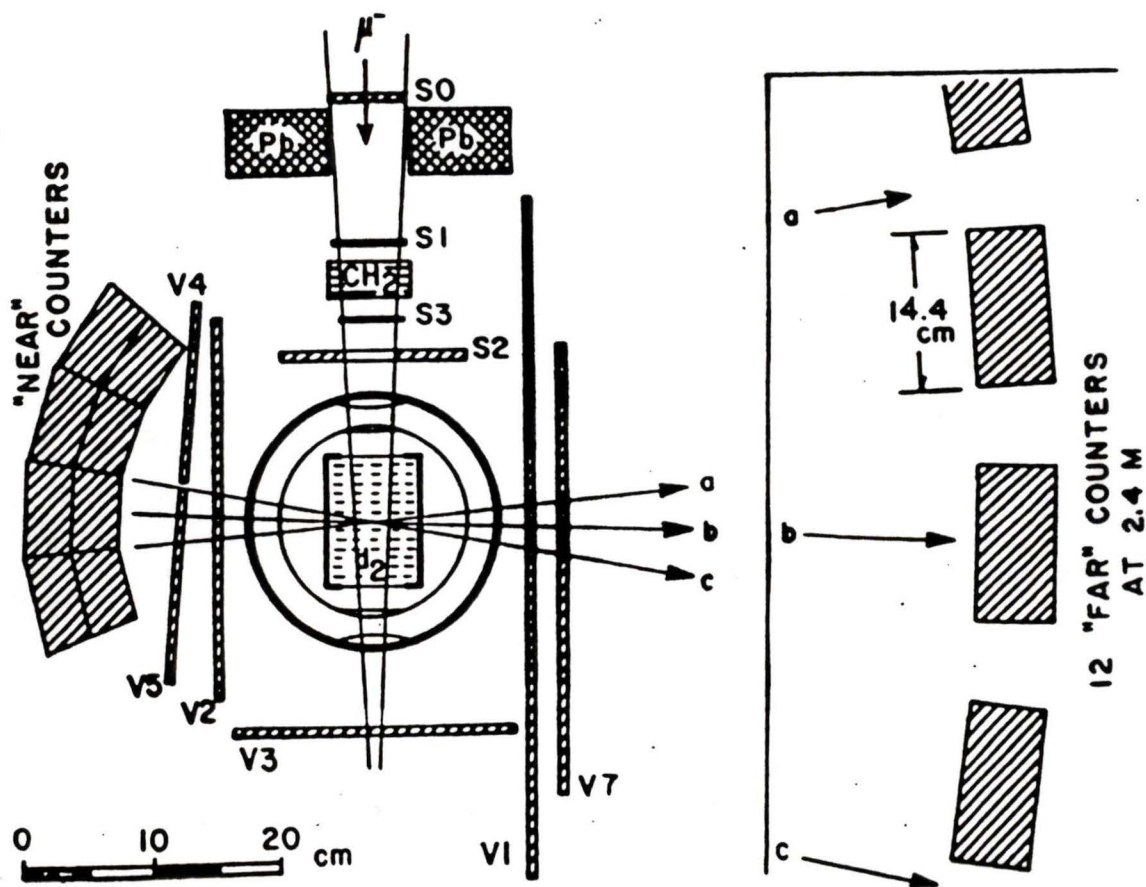


Figure 3.3: Experimental arrangement in target area showing muon telescope, veto system and neutron counters, only three of the twelve Far counters are shown for clarity.

### 3.1.1 TRIUMF M20A Channel

The experiment was performed at the TRIUMF meson facility located near the University of British Columbia campus in Vancouver. The M20A stopped muon channel was used in the backward-decaying muon mode. The layout of the channel is shown in Fig. 3.4. Muons are produced by decaying pions which originate from target T2 at an angle of  $55^\circ$  to the main beam-line 1A. The pions are produced by bombardment of T2 by 500 Mev protons that are produced by the main cyclotron. The beam then passes through a series of eleven quadrupole magnets, Q1 thru Q11 and two dipole magnets, B1 and B2. The dipoles allow momentum selection and the quadrupoles focus the beam. The total length of the channel is 9.4 m and the bends are such that the final beam emerges at approximately  $90^\circ$  to BL1A. For the purpose of this measurement, the channel was nominally tuned for 97 Mev/c muons at a momentum bite,  $\Delta p/p$ , of 9%. With an average primary unpolarized proton beam current of  $100 \mu\text{A}$  and the standard 10 cm beryllium production target at T2, the mean muon stopping rate within the target was  $96\text{K s}^{-1}$ ; in all  $3.8 \times 10^{10}$  muons were stopped. The pion and electron contamination was estimated to be less than 1%.

### 3.1.2 Liquid Deuterium Target

The liquid deuterium target, designed by Caffrey *et al.*[37], was a 7.5 cm diameter by 10 cm right cylinder with the axis of the cylinder parallel to the beam. The target assembly is shown in Fig. 3.5, the connections to the cryogenic system and vacuum chambers are shown as well. The chamber vessel was constructed of de-oxygenated high conductivity copper to eliminate bubbling due to uneven heat conduction and to insure a homogenous density distribution. The chamber was baked out at 473 K for seven days in order to achieve a vacuum of  $10^{-8}$  Torr. To ensure an ultra-pure deuterium sample in the target, commercially obtained high

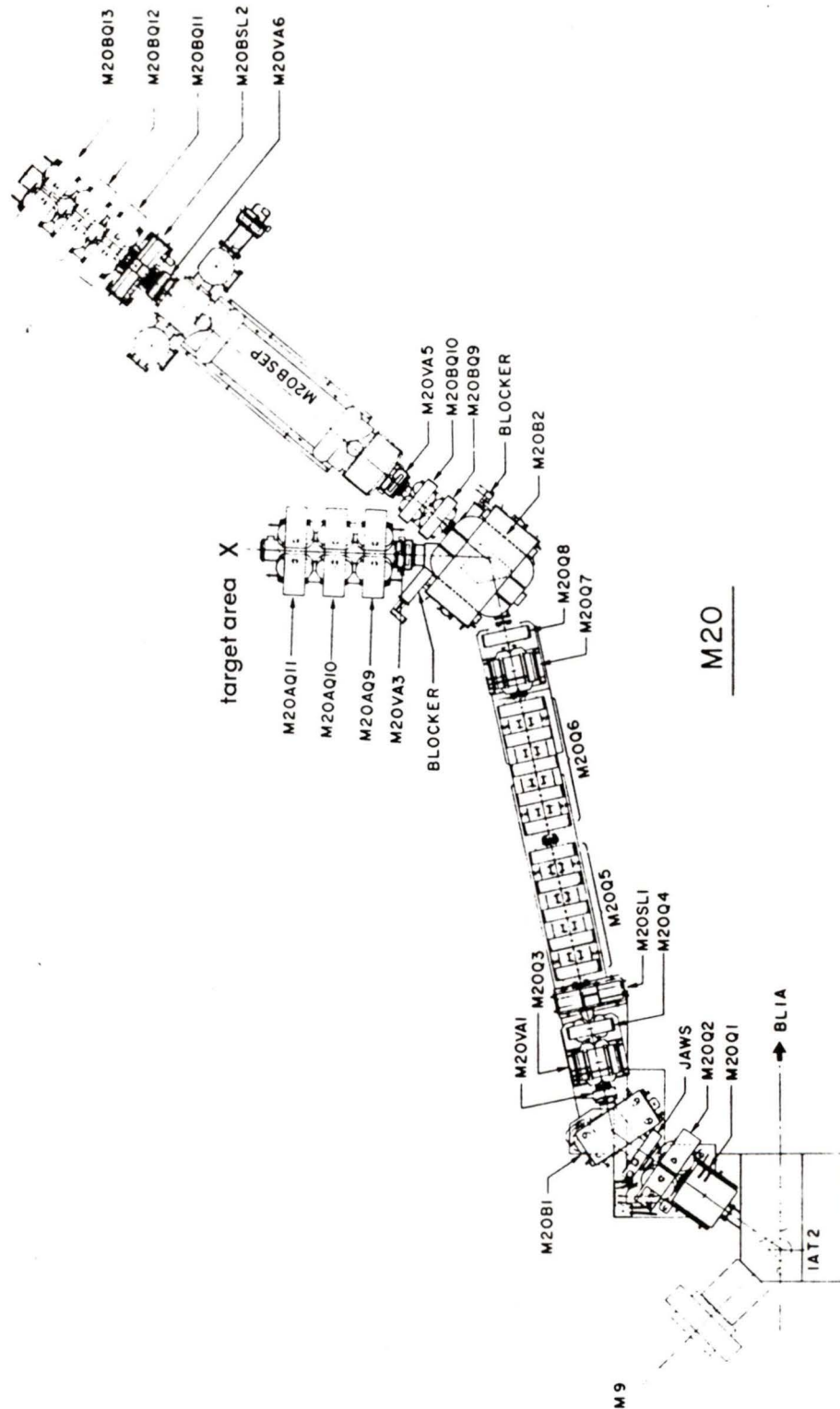


Figure 3.4: TRIUMF M20 channel, the channel divides into M20A and M20B at bending magnet M20B2.

purity deuterium gas was passed through an oxygen removal system and a high pressure (200 psi) palladium leak<sup>3</sup> which was operated at 673 K. The specifications of the palladium leak stated that the impurity level in the target should not have exceeded one part in 100 million; however, this could not be experimentally verified. The target was constructed with only high Z materials. Muons stopping in the target walls will quickly interact<sup>4</sup> and the produced background can be eliminated on the basis of event time considerations; an event within the first 100 ns of a muon stop signal has a higher probability that capture by a heavier nucleus was responsible.

### 3.1.3 Neutron Detection System

The far neutron counter array consisted of twelve (7.5 cm thick, 14.4 cm wide, 63.5 cm high) NE 110 and Pilot Y<sup>5</sup> plastic scintillators. The far detectors were placed side by side in semi-circular formation 244 cm (8') from the target. At this distance each detector subtended horizontally an angle of approximately  $5^\circ$ . The solid angle subtended by the array was 1.5% of the total  $4\pi$  steradians. The neutron detectors were large enough that the position of detection could influence the timing because of the finite time (about 3 ns from top to bottom) required for transmission of the light to the photomultiplier tube (PMT). To compensate for this, the scintillators were viewed at top and bottom by PMT's; the mean of the difference between the time-zero signal and the two stop signals was used to determine the time-of-flight.

The near neutron counter array consisted of eight smaller scintillators; 3.75 cm deep by 7.5 cm high with the width tapered slightly from back to front (7.6 to 5.1 cm) in order to improve the angular resolution of the system. Each of these scintillators were viewed with a single PMT. The

---

<sup>3</sup>Johnson Matthey Inc.

<sup>4</sup>Recall that the nuclear capture rate is  $\propto Z^4$

<sup>5</sup>Nuclear Enterprise Co.

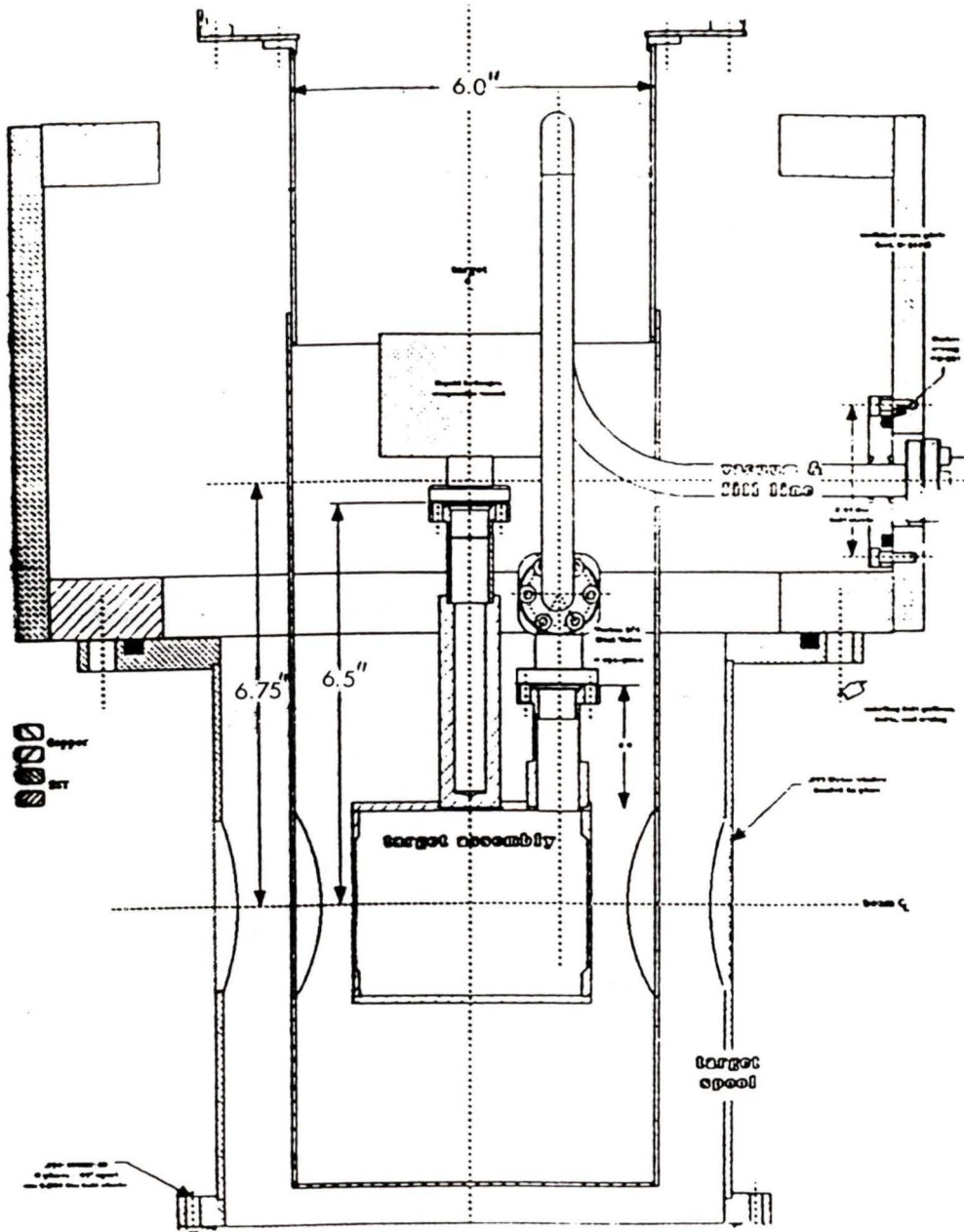


Figure 3.5: Target Assembly showing liquid deuterium target cell, designed by Caffrey *et al.*

Near counters were arranged in a four by two deep pattern as seen in Fig. 3.3. Each Near detector had associated with it three adjacent far counters to give a total angular acceptance of  $16^\circ$ .

### 3.1.4 Muon Telescope and Veto System

To determine if a muon had stopped in the target, a five element particle telescope was employed as shown in Fig. 3.3. The required signal logic to indicate a stopped particle was  $S0 \bullet S1 \bullet S3 \bullet \overline{S2} \bullet \overline{V3}$ . The first four elements, S0 thru S3, were placed upstream of the target. The fifth, V3, which also served as a veto counter for charged particles<sup>6</sup>, was placed downstream of the target.

The first two elements, S0 and S1, were each 3" wide squares and 1/4" and 1/8" thick, located at 23 cm and 12 cm, respectively, from the target window. S0 was placed at the opening of the beam pipe immediately in front of the lead collimators. S0 served to define the beam particles entering the target area; it detected particles before they could possibly scatter off the collimators and interact with the Near counters, producing spurious events. The scintillator S2 was used to reject muons that would stop near the target side wall where they could possibly interact with the target construction, it was 6" x 6" by 1/4" with a 1 5/8" diameter hole and was located 3 cm from the target vacuum box. The greater thickness was to insure a high veto efficiency. The diameter chosen was such that the defined beam was at least 1.6 cm away from the target side wall. The scintillator S3 was 2" in diameter, 1/16" thick and 6 cm upstream from the target. It detected particles in a 2" diameter section centered on the target, S3 was chosen to be thin in order to avoid low energy particles from stopping within it and generating false stop signals. There was a polyethylene, CH<sub>2</sub>, degrader placed between S1 and S3, which was used to

<sup>6</sup>These were predominately muon decay electrons.

degrade the muon's energy before entering the target assembly. The large veto counter V3, downstream of the target, was used to veto events where the particle traversed the target assembly.

To veto signals in the neutron counters due to charged particles originating from the target area, a double layer of thin (1/16") scintillators were placed between the target and counter arrays. The veto counters, V1 to V7, also served to detect the muon decay electron.

### Muon Stopping Distribution

To maximize the stopping distribution of the muons in the center of the target a variety of techniques were used. A particle telescope was aimed at the center of the target and used to detect the muon decay electrons. The CH<sub>2</sub> degrader thickness was varied and the ratio of electron telescope counts in coincidence with a muon stop ( $\mu_{\text{stop}}$ ) signal to the counts in S1 was measured ( $e^- \text{ tele.} \bullet \mu_{\text{stop}}/S1$ ). The currents in the channel quadrupoles Q9 to Q11 were varied in an attempt to focus the muon beam on the center of the target. This was done to minimize the number of events in the first 200 ns following a muon stop signal. The 200 ns activity was attributed to muons scattering into the target walls and being captured by high Z elements. This was verified by placing a 2" diameter NaI crystal detector 8" under the target to detect the muonic copper x-rays from the electromagnetic cascade. The 2  $\mu\text{sec}$  TDC spectrum is shown in Fig. 3.6. The effect of varying the magnet currents was quantitatively seen by plotting the ratio of the counts in the first 200 ns (channels 1800 to 1600) following a stop signal to those in the last 800 ns (channels 800 to 0) of the 2  $\mu\text{sec}$  gate strobed by the  $\mu$ -stop signal.

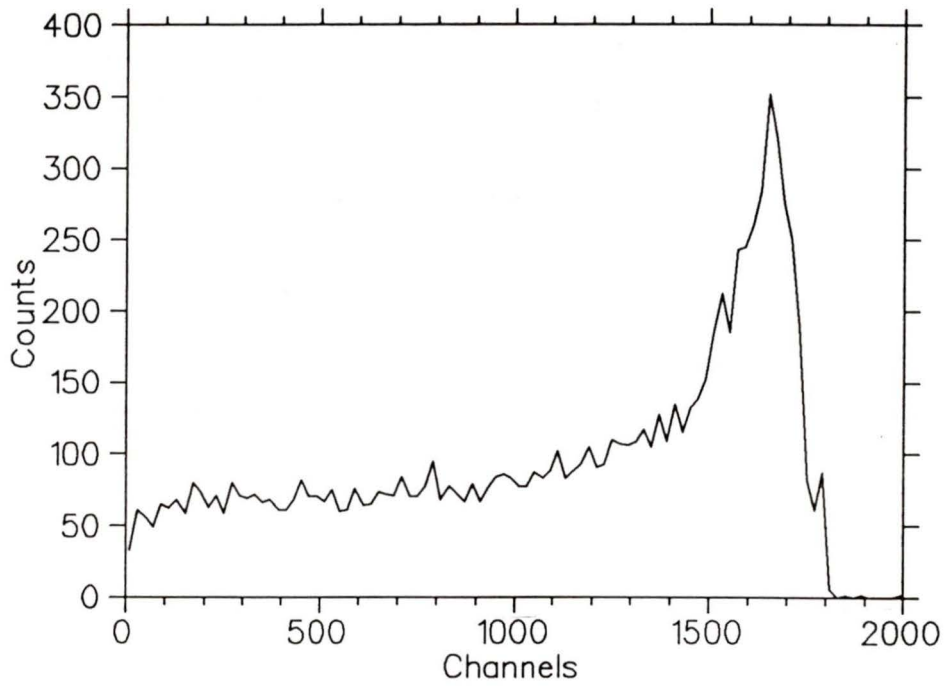


Figure 3.6: 2  $\mu\text{sec}$  TDC for all runs, the scale factor from channel number to ns approximately is 1 to 1. Note that time goes from right to left.

### 3.2 Electronics and Timing

The detailed schematics of the electronics are shown in Fig. 3.7 to 3.10. Fig. 3.7 shows the muon telescope and veto detection system; the 2  $\mu\text{sec}$  TDC and various pile detection circuits tried during the course of the experiment is shown in Fig. 3.8. The signal path for a valid Master Gate pulse is presented in Fig. 3.9. The hardwired back to back requirement is shown in Fig. 3.10; the logic for a signal in Near counter numbers 1 or 2 and a signal in Far counter number 10 is detailed. The timing at the input to the TDC's (Time to Digital Converter) for the time-of-flight system and Master Gate is shown in Fig. 3.11. The relative timing of the neutron counter signals with respect to the 2  $\mu\text{sec}$   $\mu\text{stop}$  latch are also shown in Fig. 3.11. A simplified schematic of the electronics showing the logic requirements for a Master Gate pulse and the logic for the time-of-flight TDC's is shown in Fig. 3.12.

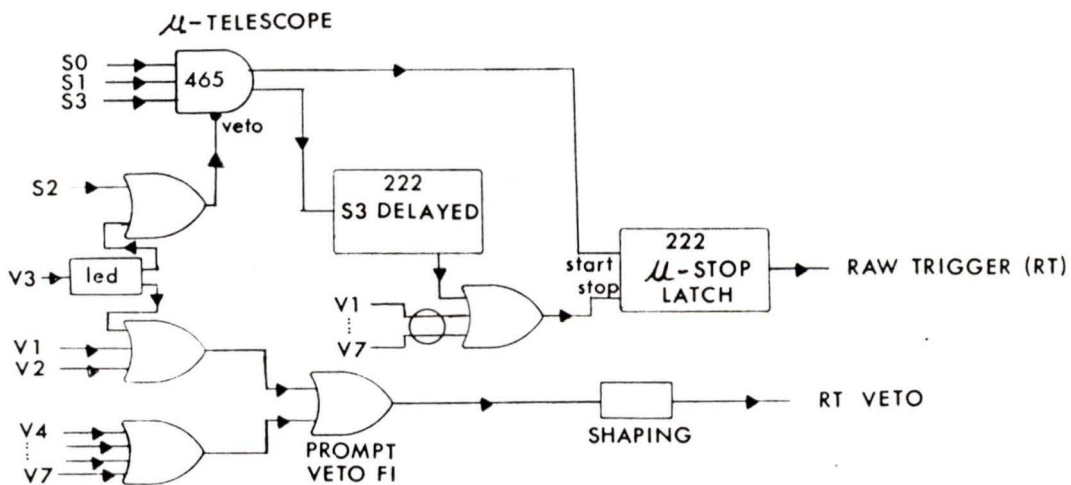


Figure 3.7: Muon Telescope and Veto System, FI refers to a fan-in and led to a leading edge discriminator.

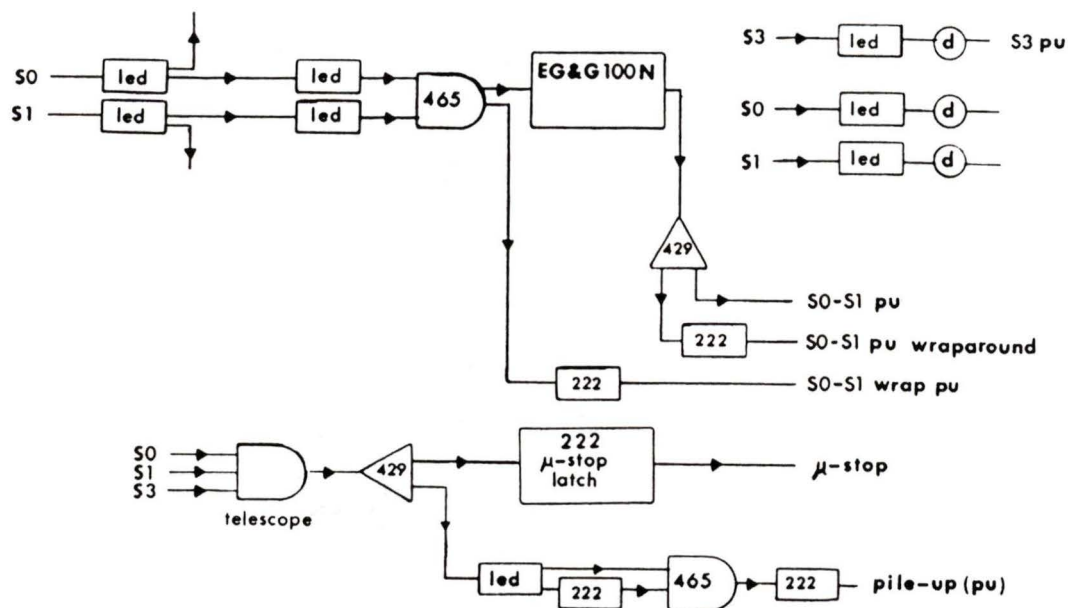


Figure 3.8: 2  $\mu$ sec TDC and pile up circuits.

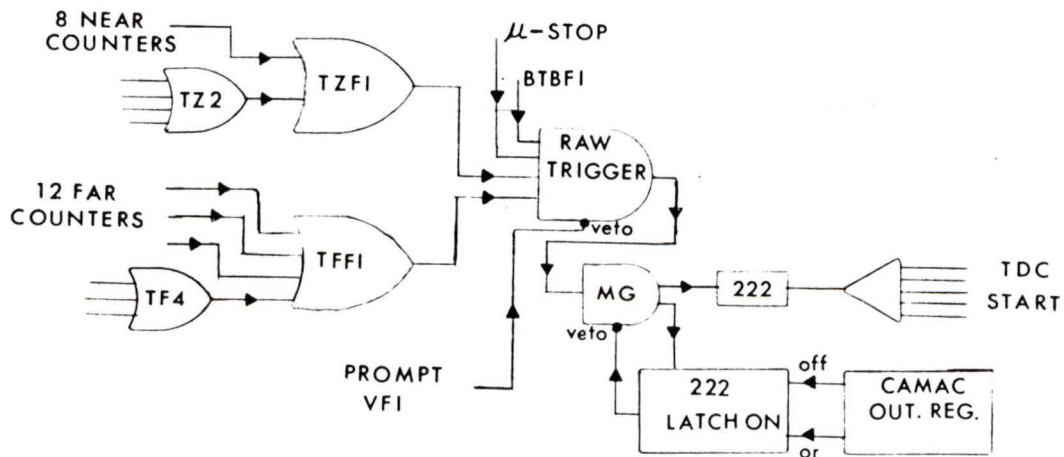


Figure 3.9: Master Gate (MG).

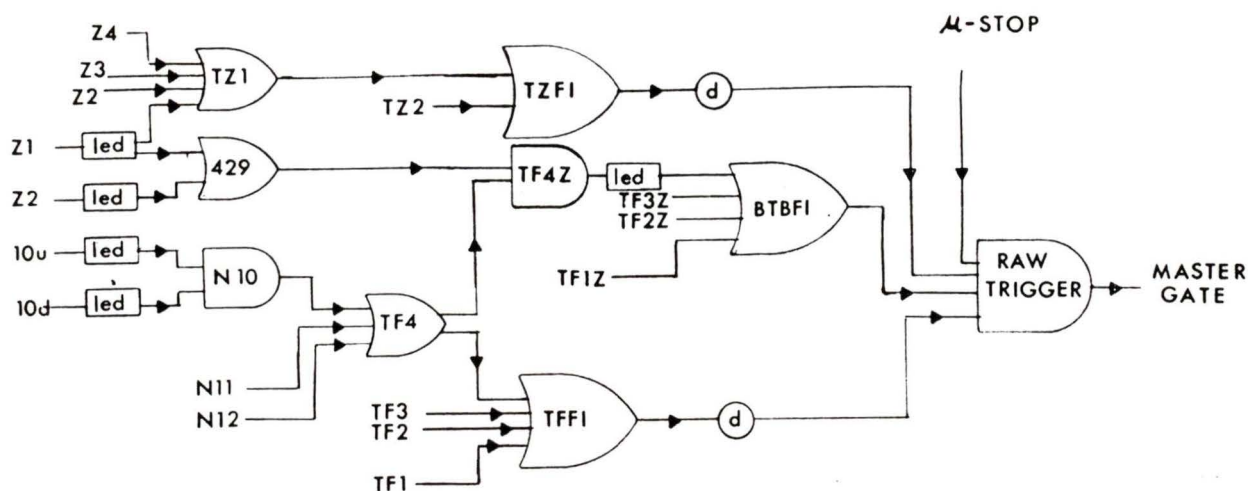


Figure 3.10: Back to Back requirement, the logic is detailed for Far counter 10 and Near counter 1 or 2.

### Calibration

The timing for the neutron counters was calibrated using the prompt  $\gamma$ -rays from  $^{22}\text{Na}$ , the back to back photons emitted providing a “speed of light” reference point. The discriminator thresholds were set using the 0.511 Mev  $\gamma$ -rays of  $^{22}\text{Na}$ . To obtain a calibration for the ADC’s (Amplitude to Digital Converter), the detector response to  $^{60}\text{Co}$   $\gamma$ -rays was measured as well. Since  $^{60}\text{Co}$  emits two  $\gamma$ -rays of similar energy and equal intensity, the average value of 1.25 Mev was used for calibration purposes. The telescope TDC’s were calibrated using a pulser for various signal delay differences. The differences corresponded to  $2^n$  ns; this was done to test the individual counting bits and the linearity of the TDC.

### Master Gate

The start input for all TDC’s was the output of the Master Gate, Fig. 3.12. The Master Gate requirement for an event was as follows:

1. stopped muon signal from particle telescope,

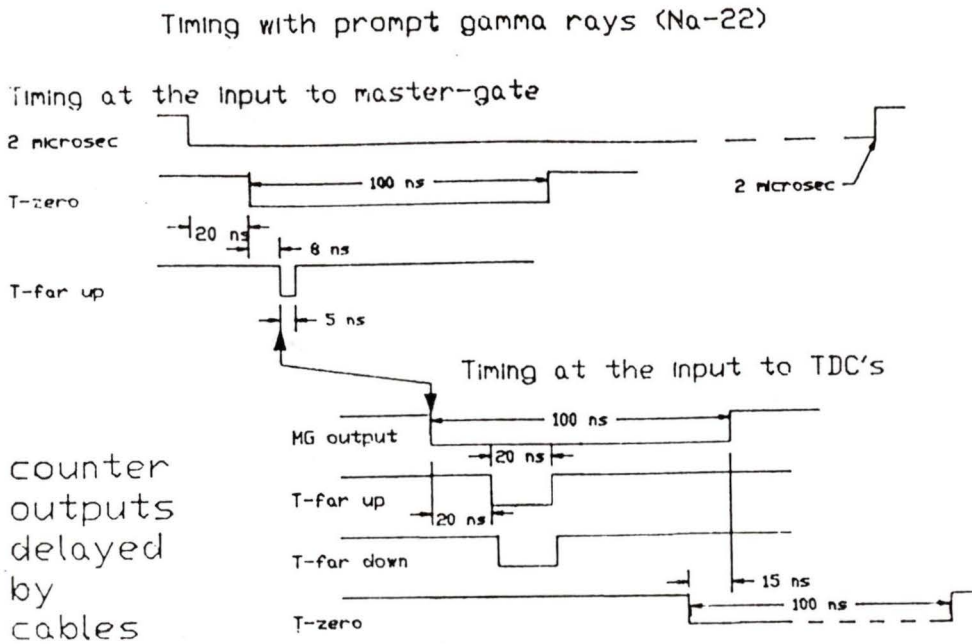


Figure 3.11: Timing at input to Master Gate and TDC's

2. coincidence between up and down PMT's in a Far counter
3. coincidence between a Near and a Far counter in the 20 ns to 2  $\mu$ -s window following a telescope stop signal,
4. absence of a prompt veto signal from either of V1 thru V7,
5. back to back firing pattern in neutron counters; This was relaxed for runs 34 through 49.

An event would be vetoed if the the data acquisition system was busy with a previous event. The Master Gate output was strobed by the Far counter up PMT pulse, as shown in Fig. 3.11. The stop signal for all TDC's were obtained directly from the counters as seen in Fig. 3.12. The stop signals were delayed in order for the logical decision to be made by the Raw Trigger leading to the 100 ns Master Gate pulse; the delay times were of the order of 200 ns.

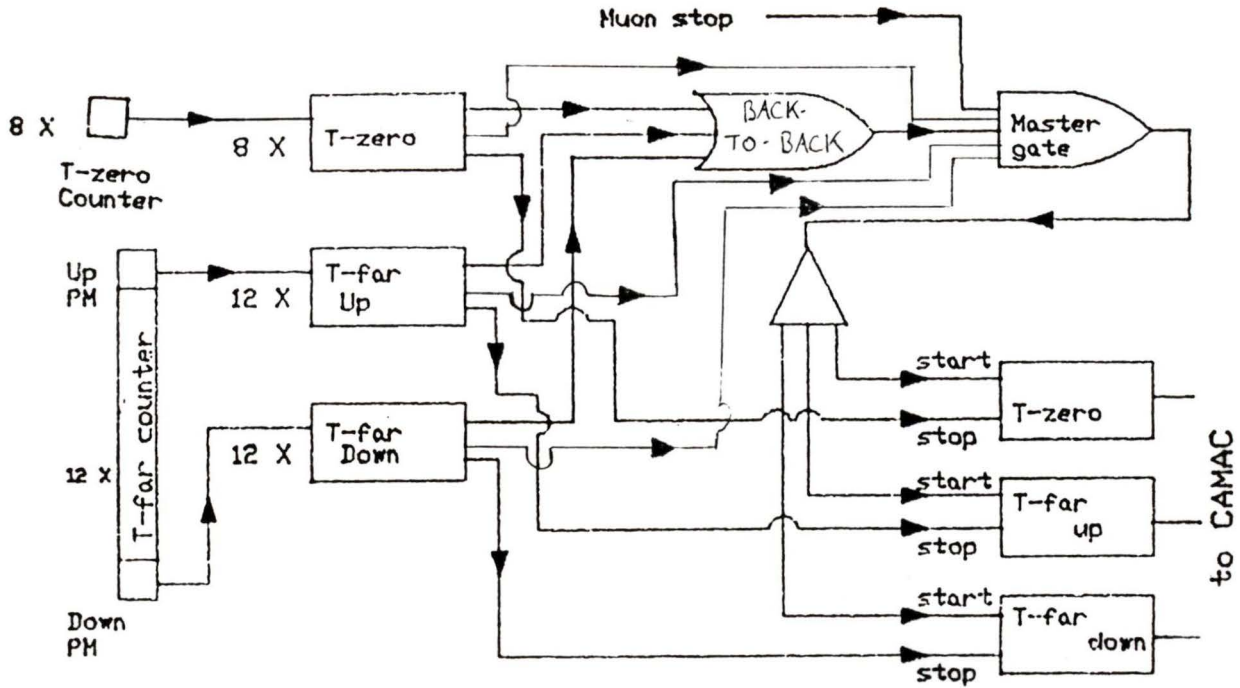


Figure 3.12: Simplified experimental schematic showing the logic at the input to the Master Gate and TOF TDC's.

### Counter Latch Patterns

The back-to-back requirement consisted of demanding that the coincidence between the Near and Far neutron counter arrays satisfy one of the following latch patterns (refer to Fig. 3.13 for counter number arrangement):

- near counters 1 or 2 in coincidence with far counters 10, 11 or 12,
- near counters 3 or 4 in coincidence with far counters 7,8 or 9,
- near counters 5 or 6 in coincidence with far counters 4, 5 or 6,
- near counters 7 or 8 in coincidence with far counters 1, 2 or 3.

Events with multiplicity in either the near or far counter arrays were recorded. The firing patterns in the neutron detector arrays were recorded

as hexadecimal 8 bit data words which were created by a C212 CAMAC register<sup>7</sup>.

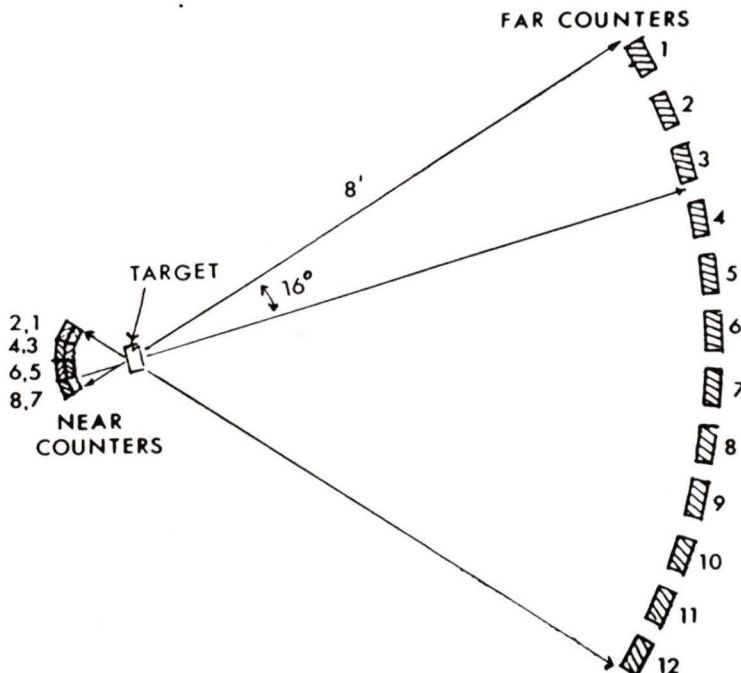


Figure 3.13: Arrangement of neutron counters showing 16° angular requirement.

### Muon Telescope and Pile-Up Detection

The output of the muon telescope coincidence,  $S_0 \bullet S_1 \bullet S_3 \bullet \overline{S_2} \bullet \overline{V_3}$ , was used as a start for a 2  $\mu$ s gate referred to as the  $\mu$ -stop latch. The latch would remain open if no signal in V1 thru V7 was present, a veto signal would cause the gate to reset, which required about 40 ns. Any further stopped particles detected within this window were recorded as pile-up events. The Master Gate output started a 2  $\mu$ s TDC<sup>8</sup> that recorded the event time in the Near counters following a stop signal. The time distribution of additional pulses in S0 within the  $\mu$ -stop latch was measured in a TDC. The start pulse for the S0-TDC was strobed by S3. An EG&G

<sup>7</sup>ORTEC Co.

<sup>8</sup>See Fig. 3.8

GP 100N pileup detection module was used for pulses from an S0•S1 coincidence. The time distribution of the S0-S1 pile-up was also recorded in a TDC. Later in the experiment, Run 42, the thresholds of S0 and S1 were set low enough to detect electrons emanating from the beam line aperture; these electrons scattering into the near counters contributed to the background.

# Chapter 4

## Analysis of Data and Results

The data were analyzed using the TRIUMF program MOLLI [38] which employs the FIOWA [39] histogramming package. The main analysis routine was written by A.J. Caffrey, and was subsequently modified by the author. The analysis was performed at the University of Victoria on a Vax 11-750. The software requirements for a valid event were:

1. back to back ( $\Delta\theta \leq 16^\circ$ ) latch (coincidence) pattern in Near and Far counters;
2. single event multiplicity in both counter arrays;
3. amplitude of signal in Near counters greater than  $3.6 \text{ Mev}_{e.e.}$ ;<sup>1</sup>
4. average of the Far counter amplitudes within a  $8.8 \text{ Mev}_{e.e.}$  and  $39 \text{ Mev}_{e.e.}$  window;
5. a  $2 \mu\text{s}$  muon telescope gate satisfying conditions as described in section 4.1.2

To fully interpret the data, the following histograms and scatterplots were generated for each of the 24 pairs of the neutron counters allowed by the latch pattern:

---

<sup>1</sup> $\text{Mev}_{e.e.}$ : Mev electron equivalent, the term is defined in section 4.1.2

1. histogram of the time-of-flight TDC spectrum;
2. scatterplot of the Near counter amplitude versus the time-of-flight;
3. scatterplot of the Far counter amplitude versus the time-of-flight.

Each of these were then summed to produce composite scatterplots and the time-of-flight spectrum. The summed TDC spectra for the front and back rows of Near counters were separately recorded as well. For events with a detected pileup, the time-of-flight vs. pileup time was plotted to determine the nature of the piled up event; the cuts on the 2  $\mu$ sec TDC were then determined by eliminating regions of the scatterplot which exhibited a high density of events that did not correspond to neutrons. Separate histograms of the pileup time and the time-of-flight for a pileup event were generated as well.

## 4.1 Analysis Technique

### 4.1.1 Calibration of TOF TDC Spectra

In order to calibrate the time-of-flight TDC spectra, several of the experimental runs were made using a stopped negative pion beam. Pion absorption at rest on deuterium,  $\pi^- + d \rightarrow n + n$ , produces a back-to-back signal of 68.03 Mev neutrons. The TOF system consisted of 24 pairs of neutron counters; for each of these pairs, the mean value of the neutron peak was located to within 0.05 ns (1 channel) of the theoretical value of 20.22 ns. The theoretical value corresponds to the time-of-flight over a 219 cm path. The timing resolution of the system was also determined from the summed neutron TOF spectra obtained from  $\pi^-$  data. A three parameter Gaussian (amplitude, mean and standard deviation) was fitted to the spectrum and a value 1.13 ns FWHM at 20.18 ns was obtained for the timing resolution and position of the neutron peak respectively. The fitted function and time-of-flight spectrum are shown in Fig. 4.1.

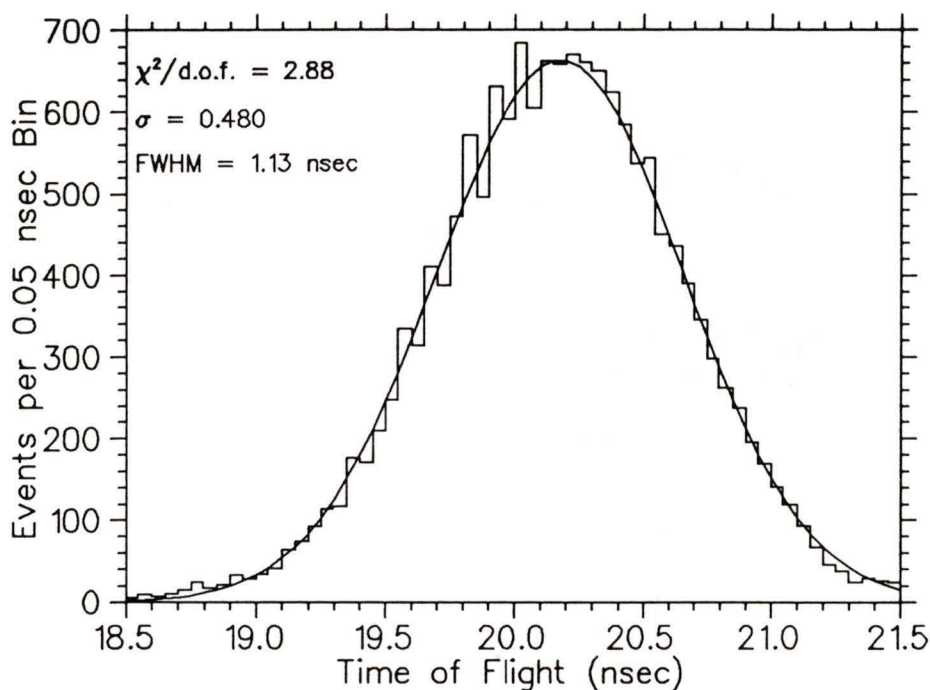


Figure 4.1: Timing resolution obtained from  $\pi^-$  data.

The amplitude of the Far counter signal was plotted versus the time-of-flight for each counter pair in a scatterplot. The pulse-height-dependent effect on the time-of-flight was determined using a linear fit for each Far counter. This is a second order correction required to compensate for the amplitude dependence of the signal on the position of detection. The time of the discriminator firing is dependent on the size of the pulse; in principle, a constant fraction discriminator (CFD) is able to correct for the time walk produced between a large pulse and one close to threshold. The applied correction is approximately one half the timing resolution of the detector; without the correction the spectrum is slightly skewed. Events with a larger pulse in the Far counters will have a shorter time-of-flight.

### 4.1.2 Calibration of ADC Spectra

The pulse height spectra of the neutron counters were calibrated using the pulse heights of  $\gamma$ -rays from  $^{22}\text{Na}$ ,  $^{60}\text{Co}$  and the neutrons produced from pion capture on deuterium. In order to provide a standard measure of the energy deposition in experiments involving neutron detection, the energy deposition in a scintillator is expressed in  $\text{Mev}_{e.e.}$ . This is because a charged massive particle<sup>2</sup> exhibits light saturation effects due to a higher ionization density when moving slowly in a scintillator [40]. The energy deposition for a proton recoiling from an incident neutron may be expressed in the equivalent amount of energy deposited by a electron according to the formula [41]:

$$L_p = -10.68 (1 - \exp(-0.07 E_p^{0.89})) + 0.929 E_p \quad (4.1)$$

where  $L_p$  is the equivalent energy of an electron and  $E_p$  is the proton energy.

The conversion factor from channel number to  $\text{Mev}_{e.e.}$  for the Near counter ADC's was obtained from the difference between  $^{22}\text{Na}$  and  $^{60}\text{Co}$  Compton edges. The obtained value was compared to the value calculated from the positions of the end points; where the end point is defined as the intersection of the straight line describing the steepest descent of the tail of the spectrum with the channel axis. Assuming a Gaussian detector response, the difference between the endpoint and the Compton edge corresponds to  $2\sigma$ , where  $\sigma$  is the detector energy resolution. The pedestal in  $\text{Mev}_{e.e.}$  was then calculated using the  $^{22}\text{Na}$  Compton edge as the calibration point. The Far counters were calibrated similarly; the signals from  $^{22}\text{Na}$  and the end point of the neutron signal from  $\pi$  capture were used. The position of the end point in the ADC spectra for the 68 Mev pion capture neutrons corresponds to the maximum energy deposition of  $53.3 \text{ Mev}_{e.e.}$ .

---

<sup>2</sup>A neutron is detected indirectly, this will be further discussed in section 4.1.3.

### Pile Up and Telescope Cuts

The cuts on the 2  $\mu\text{sec}$  gate were:

1. rejection of any event with more than one muon stop signal in the 2  $\mu\text{-sec}$  gate;
2. rejection of prompt events in the first 192 ns following a stop signal
3. vetoing of events with a signal in S0 in the first 200 ns preceding a Master Gate signal;
4. rejection of events with a S0•S1 coincidence within the 220 ns preceding a Master Gate signal.

The cuts on the telescope TDC's were determined from the scatterplots relating the pile up time to the associated time-of-flight. From this analysis, the events due to the pion contamination were eliminated. The pion capture rate on deuterium is large, about  $10^{14} \text{ s}^{-1}$  [13]; thus, pions stopping in the target will quickly be captured. The unique time-of-flight for the  $\pi^-$  capture neutrons enabled immediate identification. The 192 ns cut imposed on the 2  $\mu\text{sec}$  TDC, coupled with the hardwired cut of 20 ns, served primarily to veto events attributable to capture in the copper target. Since the mean life of a  $\mu^-$  in copper is approximately 164 ns [42]; the TDC cut eliminated about 75% of possible muon captures on Cu. A further cut on the TDC would further reduce the experimental efficiency without substantially lowering the background. For the time windows on the 2  $\mu\text{sec}$  TDC, a factor of  $0.50 \pm .02$  arises for the neutron detection efficiency from the finite counting time period. The scatterplot of the time-of-flight vs. Near counter event time is shown in Fig. 4.2; the cut in terms of channel number was 1600. The high density at  $\text{tof} = 800$  and  $\text{tmustop} = 1800$ <sup>3</sup> is due to the pion contamination in the beam.

---

<sup>3</sup>tmustop corresponds to the 2  $\mu\text{sec}$  TDC.

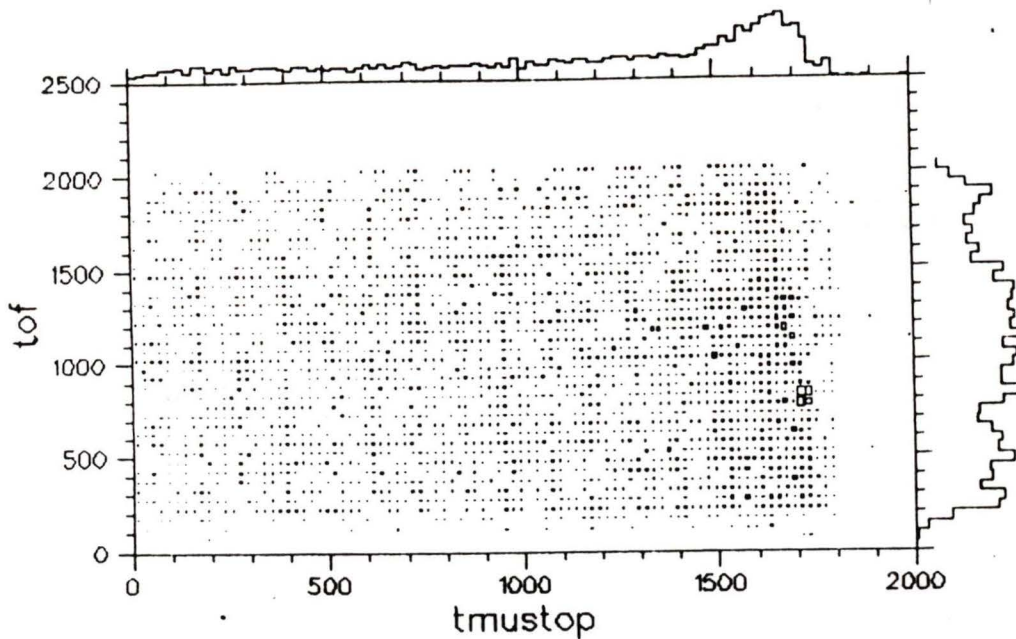


Figure 4.2: Time-of-flight vs.  $2 \mu\text{sec}$  TDC, axes expressed in arbitrary units.

Only a fraction (40%) of the data was taken with scintillator S0 in place. The need for it was not realized until well into the experiment. A histogram showing time of flight for an S0 200 ns TDC pileup shows a peak that corresponds to a speed-of-light event; the explanation is that a beam electron is scattered in such a way as to miss the veto system and to emit bremsstrahlung photons which are then detected in the counter arrays. This source of background may be eliminated by increasing the detector thresholds; for a  $5.6 \text{ Mev}_{e.e.}$  Far counter threshold, the peak in the S0 200 ns TDC pileup time-of-flight spectrum is much more prominent than for the case of an  $8.8 \text{ Mev}_{e.e.}$  threshold. The TDC cut could be applied, however, only to the last 20% of the acquired data.

### 4.1.3 Analysis Leading to the Energy Spectrum

#### Geometric Efficiency and Energy Resolution

The geometric efficiency of the TOF system was  $(1.5 \pm 0.1) \times 10^{-2}$ ; this was computed from the solid angle subtended by the Far counter array. This was unaffected by the solid angle subtended by the Near counters, only the Far counters determined the efficiency because of the coincidence requirement.

For a given neutron energy the effect of the variation in the time-zero signal, as outlined in chapter 3, was calculated. The curves in Fig. 4.3 represent the variation in the time-of-flight for a given neutron energy. Equation 3.1 was solved with  $E_1$  corresponding to the Far counter neutron

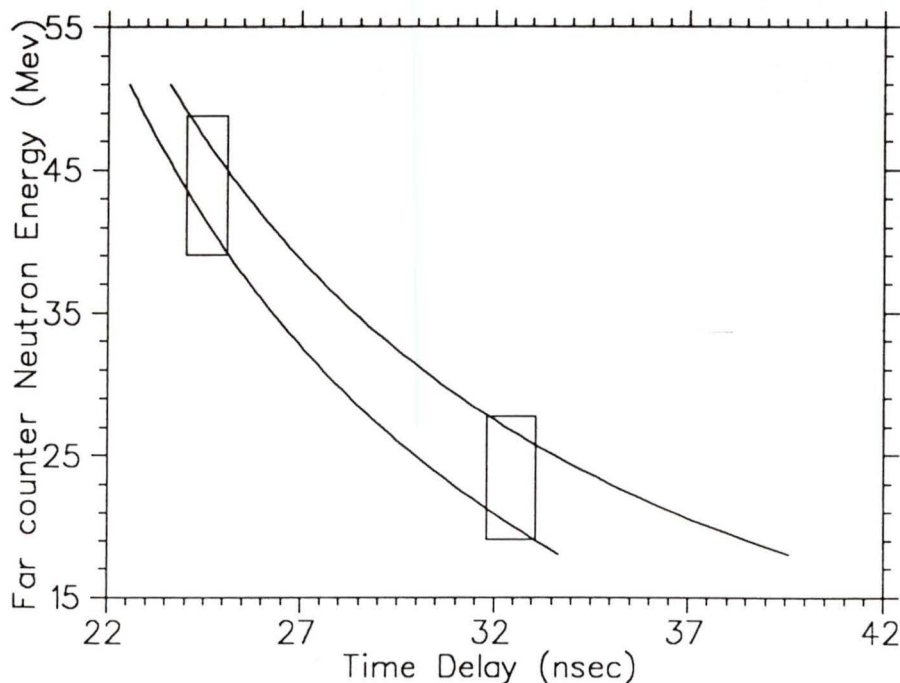


Figure 4.3: Energy resolution, kinematic and finite counter thickness effects. The 1.1 ns timing resolution is superimposed as boxes.

energy and  $E_2$  to the Near counter neutron energy. For the purposes of calculating the time spread due to kinematics,  $\theta_{nn}$  was taken to be  $180^\circ$ ;

the two solutions obtained for  $E_2$  for a given  $E_1$  were then used to calculate the time-of-flight for the Near counter neutron. The resulting values for the time delay between events in counter arrays was then used to calculate the curves in Fig. 4.3. The effects of the finite thickness of the neutron counters and target have been included. The effect of the timing resolution on the energy resolution is shown by means of superimposed boxes corresponding to the inherent timing resolution of the detectors; the effect of the timing resolution should be added in quadrature.

### **Neutron Detection Efficiency; GRACE**

The detection of neutrons is not as straightforward as that of charged particles. A neutron does not interact electromagnetically with the detector and hence a neutron is detected indirectly. In a plastic hydrocarbon scintillator, the neutron scatters elastically off a proton (hydrogen nucleus) or interacts inelastically with a carbon nucleus; the energetic charged by-products of the interaction are detected. The cross-sections for the interactions are functions of the neutron energy; thus, so are the detection efficiencies. The efficiencies also exhibit a strong dependence on the pulse height threshold; the energy deposited is not well defined for a given neutron energy.

The neutron detection efficiencies were computed using the Monte Carlo program GRACE [43]. The code has been tested for scintillators similar to those employed [44] to within 5%. The program takes into account inelastic n-carbon scattering and multiple neutron scattering effects; relativistic kinematics are employed. The calculated efficiencies for the detector thresholds employed are shown in Fig. 4.4.

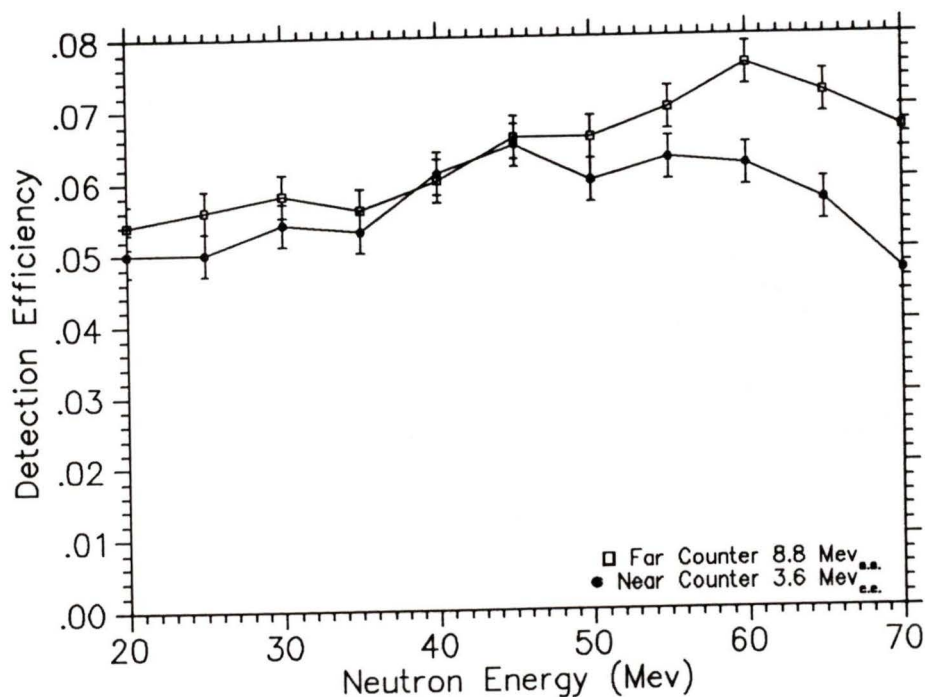


Figure 4.4: Neutron detection efficiencies, output of GRACE.

### Threshold Determination

To help determine the thresholds for the amplitudes in neutron counter arrays, the time-of-flight was plotted versus the counter amplitude. The two-dimensional histograms for the sum of the Far and of the Near counters are shown in Figs. 4.5 and 4.6, respectively. The kinematic region of interest lies between channels 850 and 1050 (time-of-fl axis). From time-of-flight considerations, the dense field of points in Fig. 4.5 near channel 600 (time-of-fl axis) corresponds to a  $\gamma - \gamma$  peak. For the Far counters, windows were imposed on the allowed pulse height. The lower threshold, 8.8 MeV<sub>e.e.</sub>, was arrived at by trying to minimize the  $\gamma - \gamma$  peak in the scatterplots without affecting the longer time-of-flight events attributable to capture neutrons. The 39 MeV<sub>e.e.</sub> threshold eliminated events with an energy deposition greater than the maximum defined by the MeV<sub>e.e.</sub> energy of a 55 MeV neutron.

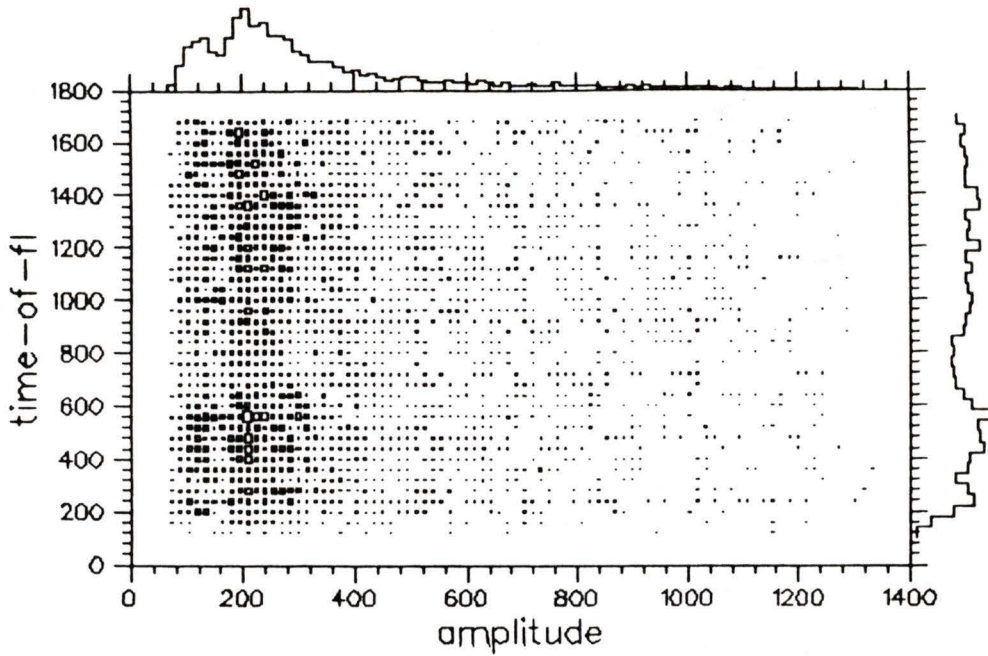


Figure 4.5: Time-of-flight vs. amplitude of Far counters, arbitrary units.

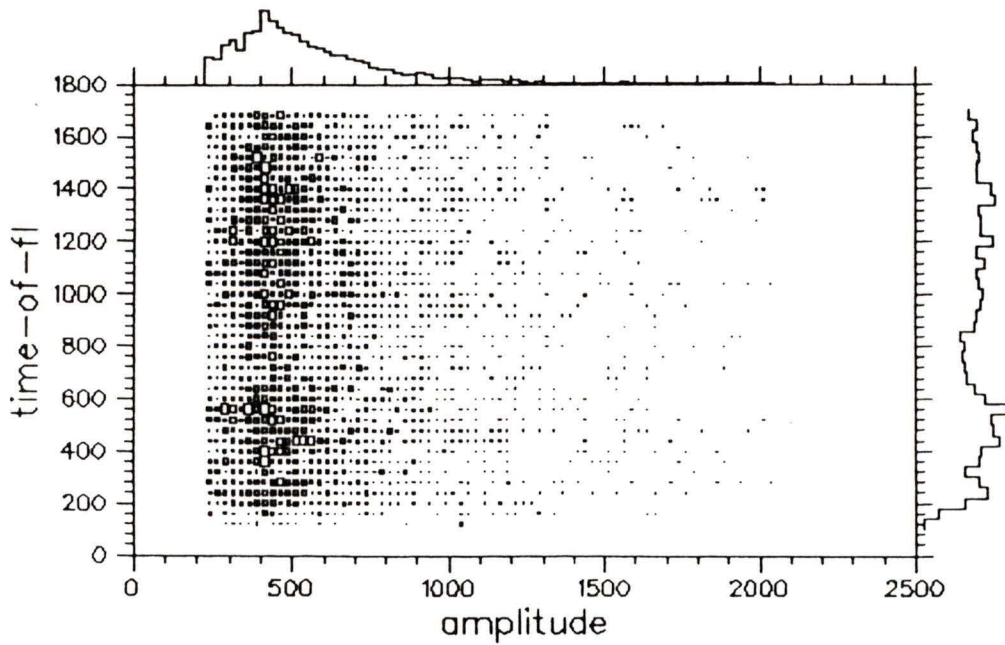


Figure 4.6: Time-of-flight vs. amplitude of Near counters, arbitrary units.

The thresholds for the Near counters were likewise determined. The baseline for the Near counter ADC's was such that the maximum pulse height for a neutron of interest was off-scale. The low energy cut, 3.6 Mev<sub>e.e.</sub> was less than that of the Far counters to take into account the wide range of neutron energies triggering the time-zero signal. From the allowed kinematics, it can be seen in Fig. 3.2 that for a 45 Mev neutron, taking into account the timing resolution, the Near counter neutron energy could range from 25 to 45 Mev.

The bulk of the  $\gamma$ -ray background could be eliminated by increasing the thresholds of the Near counters above 7.0 Mev<sub>e.e.</sub>; however, this introduces an effect on the neutron spectrum. The detection of a 20 Mev neutron in the Far counters corresponds to the detection of a similar energy neutron in the Near counters, the average energy deposition for a 10-30 Mev neutron overlaps the energy deposition from the  $\gamma$ -ray background. The effect on the spectrum cannot be reliably compensated for by Monte Carlo techniques. This because the uncertainty in the number of photo-electrons collected at the anode has a large effect on the calculated efficiencies. The computed efficiencies are not reliable below about two times the threshold setting; *i.e.*, where the average energy deposition for a recoil proton is less than twice the threshold value [43, Cecil *et al.*]

### Finite Target Effect

The finite muon stopping distribution within the target affected the coincidence probability for the back-to-back detector geometry. This was due to the strict back-to-back requirement on  $\theta_{nn}$ . To correct for this effect on the spectrum, a Monte Carlo simulation of the detector response to the effects of a finite target was performed.

The program, MONTY<sup>4</sup>, computed the coincidence efficiency of the neutron counter array using the following inputs:

---

<sup>4</sup>Monte Carlo computer programme written by the author.

1. Far counter neutron energy,
2. the position of capture event within the target,
3. the position of detection for the neutron in the Far counter array,
4. the relative angle of the neutron momenta, the limits of which were determined from equation 3.1.

If a coincidence between the counter arrays resulted, then the position of the event in the Near counters was computed to find the corresponding counter number. The resulting coincidence pattern was then compared to the experimentally allowed counter firing pattern for an accepted event. Events not satisfying this criteria were rejected.

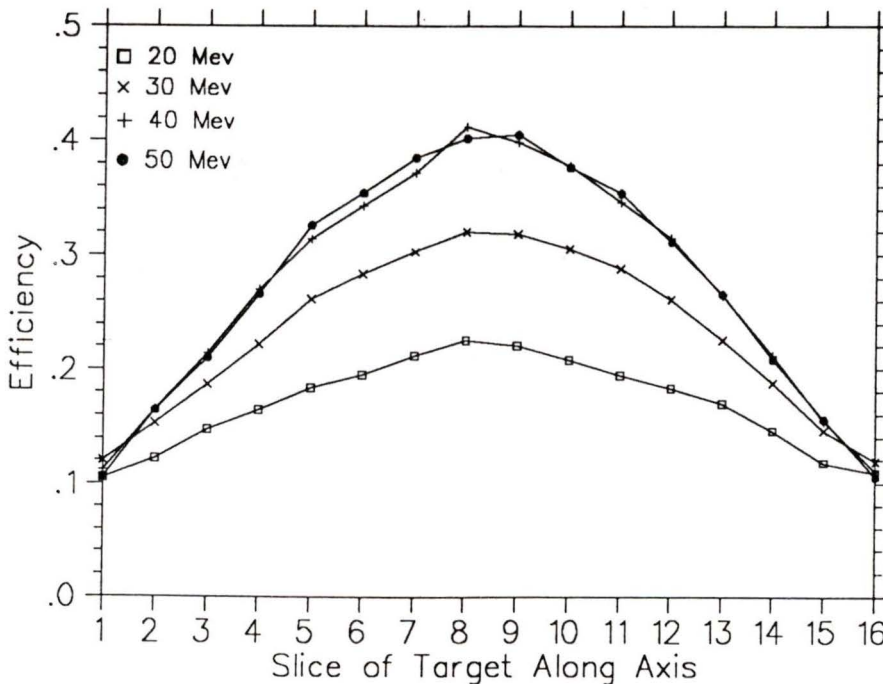


Figure 4.7: Finite target volume effect, coincidence efficiency as a function of position along target axis for different neutron energies.

The target was divided in 16 equal slices along its main axis and for each slice 10000 events were simulated. The coincidence efficiency as a

function of position along the target axis for fixed neutron energies is shown in Fig. 4.7; each slice is 0.625 cm. Note that detection efficiency is highly dependent on the distance from the center of the target and also shows a strong energy dependence.

The systematic error in the correction factor arising from this effect is primarily due to the uncertain knowledge of the stopping distribution along the target axis. The polar stopping distribution can be assumed to be isotropic, at least to the 2.1 cm radius defined by the scintillator S2; this may be concluded because of the beam spot size (about 10 cm FWHM) is much greater than the cross-section of the target defined by S2. The distribution along the target axis cannot be defined as precisely. To determine the effect of different stopping distributions on the coincidence efficiency, the following distributions were tested:

1. gaussian distribution,  $\sigma = 2.54$  cm,
2. gaussian distribution,  $\sigma = 3.81$  cm,
3. gaussian distribution,  $\sigma = 5.08$  cm, and
4. uniform along entire target length.

The efficiencies as a function of energy for the above distributions are shown in Fig. 4.8. The relatively large momentum bite (9% at 97 Mev/c) for the muon beam points to the conclusion that the stopping distribution within the target was not highly localized. As well, the degrader thickness was varied a number of times in the course of data acquisition; the variation in thickness was from 7/8" to 1 1/2". The actual stopping distribution was most likely between the two extremes of  $\sigma = 2.54$  cm and uniformity along the entire target length. The correction factors, as applied to different energies used in the normalization of the neutron spectrum, were those for the assumption of a Gaussian distribution with  $\sigma = 3.81$  cm. The

systematic error associated with this assumption was estimated to be the difference between the values for  $\sigma = 3.81$  cm with those for  $\sigma = 2.54$  cm and the uniform distribution.

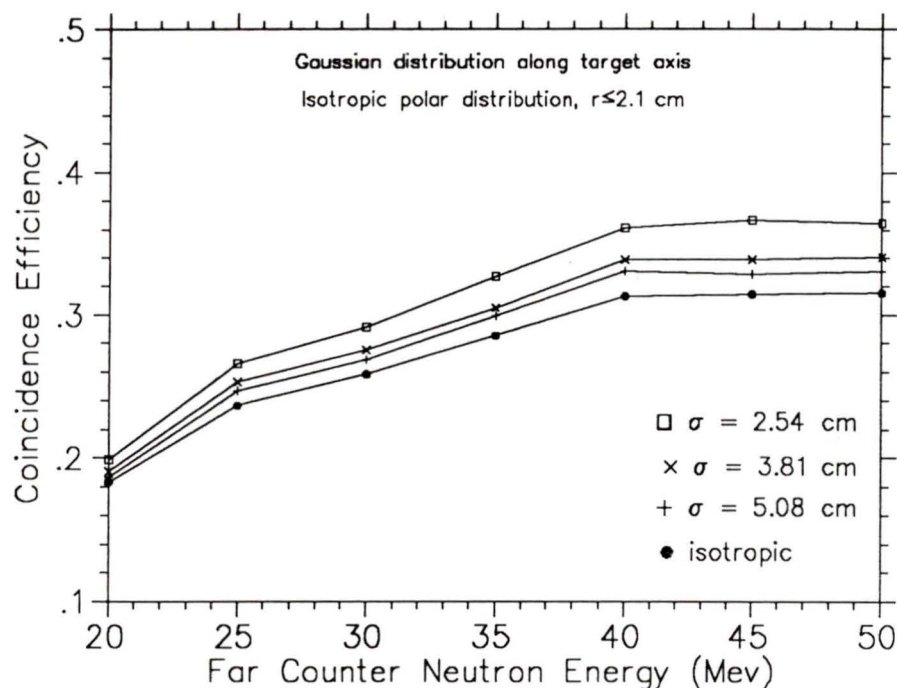


Figure 4.8: Integrated coincidence efficiency for various stopping profiles.

### Efficiency Corrections for the 2 $\mu$ sec TDC

The cuts on the 2  $\mu$ sec TDC imposed additional corrections on the final spectrum.

1. Events with 2 or more  $\mu$ -stop signals within the 2  $\mu$ sec gate were recorded and rejected; the fraction  $0.84 \pm .02$  of the events leading to a Master Gate pulse survived this cut.
2. S0-S1 pileup rejection; a factor of  $0.98 \pm .02$  arises from this.
3. The finite counting period (1.69  $\mu$ s compared to the 2.2  $\mu$ s muon life-time) introduced a correction of  $0.50 \pm .02$ .

4. Rejection of events with a S0 signal within 200 ns of a Master Gate pulse. This introduces a correction of  $0.97 \pm .02$ .

The net effect of these corrections on normalization of the spectrum was a factor of  $0.40 \pm .03$  in the overall experimental efficiency.

#### 4.1.4 Discussion of the Background

The raw time of flight spectrum before background subtraction is shown in Fig. 4.9. The kinematic region of interest is the 22 to 33 ns region<sup>5</sup> Immediately to the left of the neutron cut off (22 ns), a reasonably flat portion is evident; in this interval the coincidences are purely accidental, *i.e.* they have a random correlation.

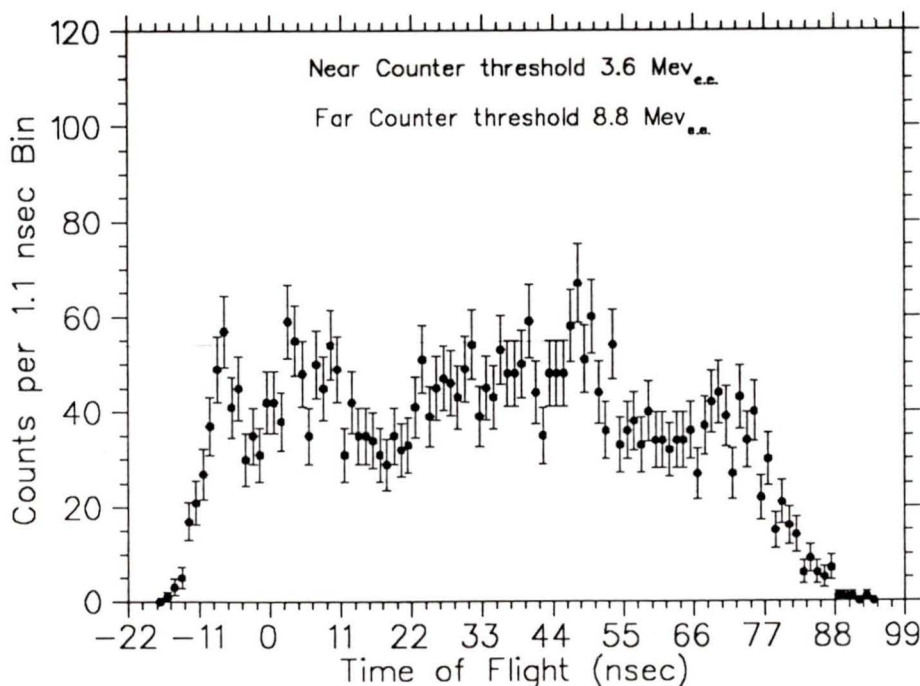


Figure 4.9: Raw time-of-flight spectrum used to obtain final energy spectrum showing background level.

<sup>5</sup>Note that energy increases from right to left, the flight times of 22 and 33 ns correspond to 54 and 25 Mev neutrons respectively

The time-of-flight spectrum shows a peak near 7.5 ns which corresponds to correlated back to back  $\gamma$ -rays being emitted from the target area. These  $\gamma$ -rays are attributed to bremsstrahlung from muon decay electrons. A  $\mu^-$  decay electron is energetic enough to produce several high energy photons; this would give rise to the  $\gamma - \gamma$  peak being slightly widened due to the finite time between interactions leading to brehmstrahlung radiation. To the left of the  $\gamma - \gamma$  peak is a peak with a shoulder extending to -1.5 ns; from time considerations this corresponds to correlated  $\gamma - n$  events, with the neutron detected in the Near counters and the  $\gamma$  detected in the Far counters. The extent of the shoulder into the negative time delay is in fair agreement with the thresholds of the Near counters; the Near counter threshold was such that neutrons of less than 7 Mev kinetic energy should not be detected; the shoulder edge corresponds to 5 Mev neutrons assuming that the neutron and  $\gamma$ -ray were emitted simultaneously from the center of the target.

The presence of a significant number of counts at the end of the spectrum in the negative time region does not have a kinematically plausible explanation. However, the presence of a similar structure, though not as well defined, at the opposite end of the spectrum supports the interpretation that the peaks are due to an electronics phenomenon related to the pulse edges of the Master Gate.

In order to determine the background level in the kinematic region of interest, the thresholds of the Far counters were increased while keeping the Near counter thresholds constant. Comparison of Fig. 4.9 with Fig. 4.10 and Fig. 4.11 shows strong evidence of additional background structure above the level defined by the 11 to 22 ns region. In Fig. 4.10, where the Far counter threshold was 6.8 Mev<sub>e.e.</sub>, there is a reasonably flat portion extending from 52 to 66 ns; however, the level is consistently higher than that in the 11 to 22 ns range. The 6.8 Mev<sub>e.e.</sub> cut corresponds to 12.5 Mev neutrons; the corresponding time-of-flight is 45 ns. The assumption

of a flat background implies that there should be no structure present in the 45 to 66 ns region; the number of counts in the two regions should be consistent with each other; Although, the statistics are poor, the respective mean values of the levels in the different regions do differ by close to  $2\sigma$ . The effect is even more dramatic in the time-of-flight spectrum shown in Fig. 4.11, where the detector threshold was 5.6 Mev<sub>e.e.</sub>. The time-of-flight spectra with the threshold cut at 8.8 Mev<sub>e.e.</sub>, Fig. 4.9, also exhibits this plateau; but, the level is consistent with the level in the 11 to 22 ns region.

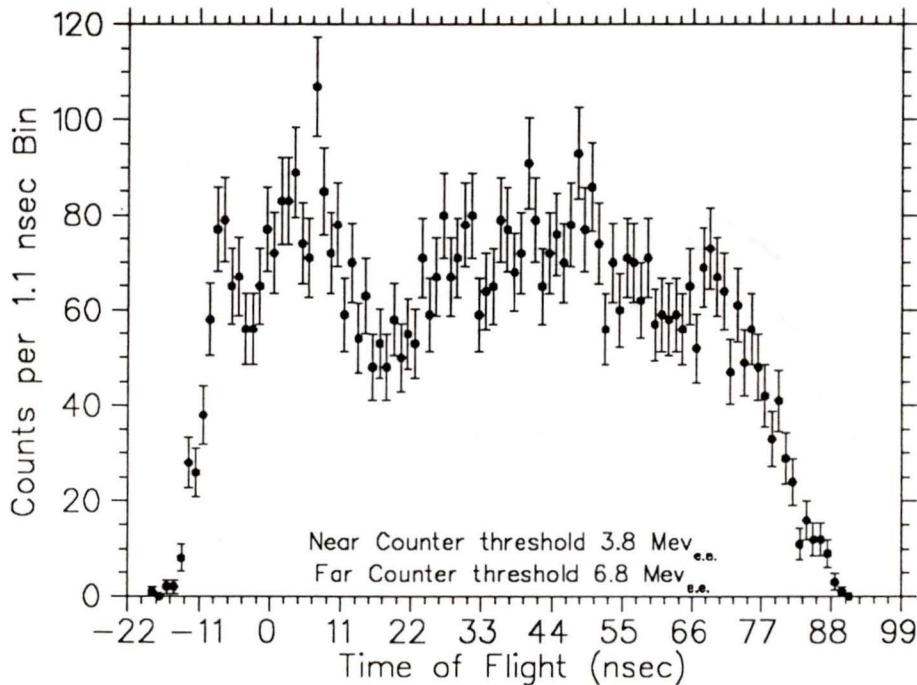


Figure 4.10: Raw time-of-flight spectrum showing background level.

The interpretation of the different background levels is that the higher level of background is due to correlated  $\gamma - n$  events; but, with the gamma ray detected in the Near counters and the neutron detected in the Far counters. Because the  $\gamma$ -ray will generate a consistent time-zero signal and the time-of-flight for neutrons detected in the Far counters will exhibit a wide variation (30 ns difference between 10 Mev and 50 Mev neu-

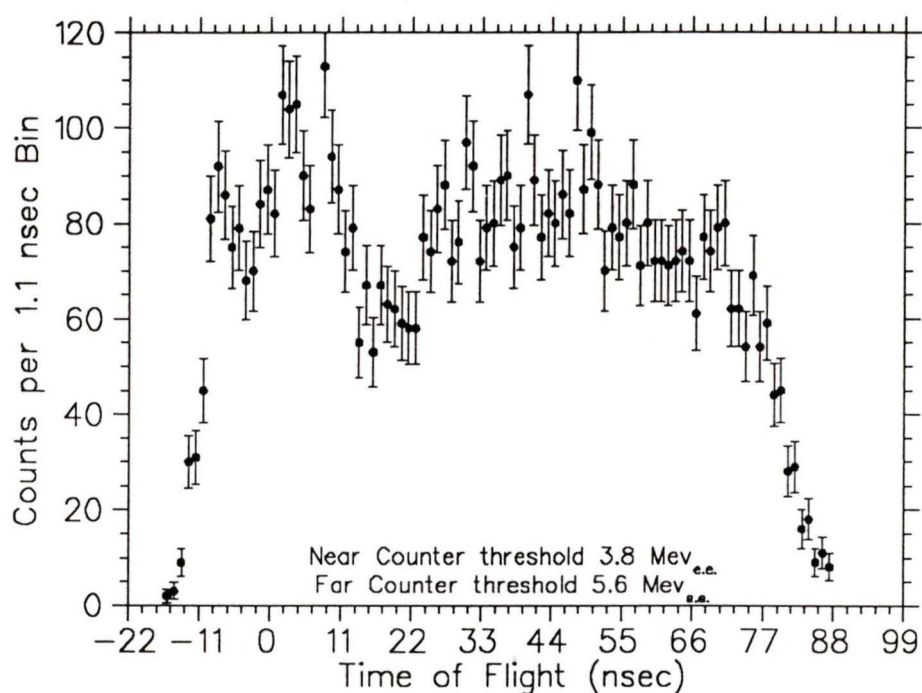


Figure 4.11: Raw time-of-flight spectrum showing background level.

trons), the resulting spectral structure will be spread out. The opposite holds true for the case of a neutron in the Near counter and a gamma in the Far counter, hence the observed peak. It must be added that the poor statistics do not favour further analysis of the background, *i.e.* fitting of various functions to determine the level of background in the kinematic region of interest.

There is evidence that there is periodic structure in the time-of-flight spectrum. The presence of a peak at 46.2 ns in each of the spectra is in agreement with the 43 ns cyclotron beam period and the  $\gamma - n$  peak located at 3.3 ns. The presence of the peak at 46.3 ns is not consistent with the threshold cuts of 8.8 Mev<sub>e.e.</sub> and 6.8 Mev<sub>e.e.</sub> which both imply that the number of counts in this region should be consistent with the 11 to 22 ns interval. The cutoff for the 6.8 Mev<sub>e.e.</sub> threshold corresponds to a 25 ns time-of-flight. This hypothesis is further supported by the observation in

Fig. 4.9 of a narrow valley immediately adjacent to the peak at 41.8 ns. The position of the valley is in fair agreement with the threshold value (8.8 Mev<sub>e.e.</sub>) limit of 40 ns. These events are attributed to beam electrons that entered the target area missing detection by the telescope system and subsequently producing bremsstrahlung  $\gamma$ -rays. It should be stressed that the thresholds on the telescope scintillators were not lowered to detect electrons until well into the experiment.

The large 2.44 Mev neutron background due to  $\mu^-$  catalyzed fusion was eliminated by proper setting of detector thresholds; the maximum height pulse for a fusion neutron being 0.75 Mev<sub>e.e.</sub>. The  $^3\text{He}$  produced in the fusion process<sup>6</sup> has two effects on the measurement: a depletion of the available muons via capture by the helium nucleus and the subsequent possible energetic neutron emission. The disappearance rate due to  $^3\text{He}$  has been calculated for a liquid deuterium target [6] using two independent methods; the average value is  $48 \pm 18 \text{ s}^{-1}$ . The energetic neutron background due to capture on  $^3\text{He}$  is negligible because the partial capture rate leading to neutrons in the final state is roughly 1/4 of the total capture rate<sup>7</sup>; furthermore, the final state most likely to give rise to an energetic back-to-back event has the neutron being accompanied by an energetic deuteron, which, considering the high efficiency of the veto system for charged particles originating from the target, will be vetoed. The other possible capture channel with neutrons present is a four-body final state. The differential capture rate for energetic neutrons ( $> 25 \text{ Mev}$ ) is negligible within the context of this measurement.

---

<sup>6</sup>See section 2.1.1

<sup>7</sup>See Chapter 5, Section 2.1

### 4.1.5 Neutron Energy Spectrum

The neutron energy spectrum was calculated from the raw time-of-flight spectrum obtained using the 8.8 Mev<sub>e.e.</sub> Far counter thresholds. The subtracted background was assumed to be flat; the level was determined from the 11 to 22 ns and 53 to 67 ns regions. The theoretical spectrum used for comparison was calculated assuming that the capture process was exclusively from the  $\mu d$  1S doublet state. This assumption is supported by the findings of the latest capture rate experiment performed with a liquid deuterium target [6].

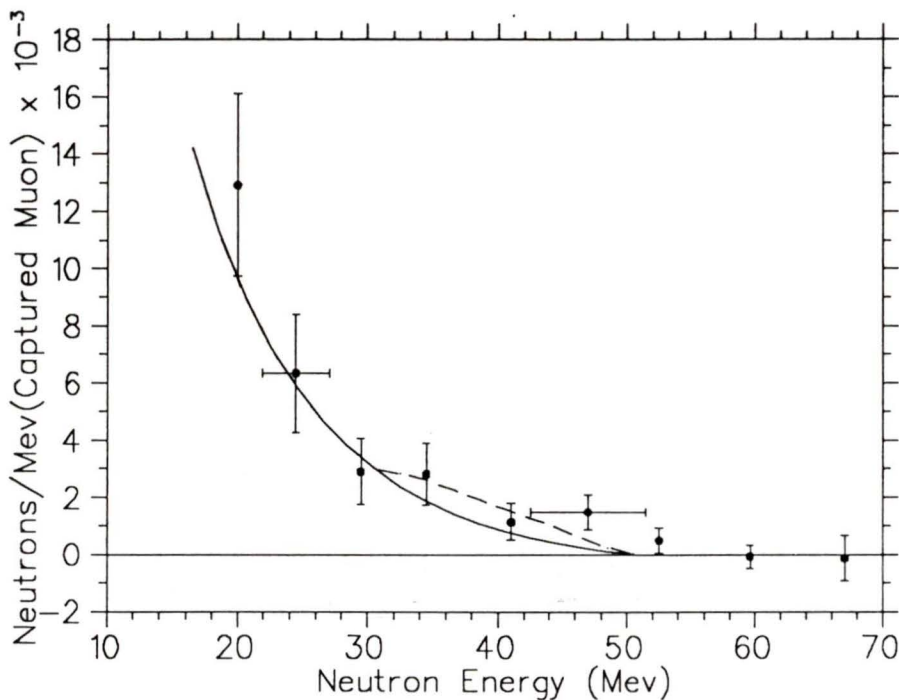


Figure 4.12: Neutron Spectrum, See text for description.

The final neutron spectrum obtained is shown in Fig. 4.12. The error bars represent only associated statistical error; the systematic error is estimated to be 15 to 20%, with the uncertainties in the muon stopping distribution and neutron detector threshold values being the dominant sources. The solid smooth curve represents the spectrum calculated using

the elementary particle technique based on the assumption of an analytic continuation of the axial vector form factor in the time-like region [13]; the dashed line represents the included effect of meson exchange currents over a 20 Mev range of neutron energies. The measured spectrum is in good agreement with theory in the 25-30 Mev range. The data point at 52 Mev is to be considered part of the neutron spectrum when the energy resolution is taken into account. In the higher energy part of the spectrum, the spectrum is within statistical agreement with theory; however, at 47 Mev there is an enhancement at the two sigma level. The agreement with theory is improved when the MEC effect is taken into account. The high statistical uncertainty does not allow an indisputable interpretation of the results; though, there is evidence of an enhancement.

# Chapter 5

## Extensions of the Experiment

Considering this experiment was the first attempt to measure any portion of neutron spectrum after muon capture on deuterium, there is room for significant improvement. The experience has shown that despite the back-to-back requirement, the background level is still high. A new proposal to measure the neutron spectrum has been prepared [45]; the proposal outlines improvements that would decrease the background significantly without sacrificing the counting rate. The improvements as put forth in the proposal will be presented along with suggestions by the author that followed the submission of the proposal.

Recently a proposal to measure the fast neutron spectrum following muon capture on liquid  $^3\text{He}$  and  $^4\text{He}$  was submitted [46]. A measurement for helium would complement the work done with deuterium to the extent that MEC effects on energetic neutron emission for three and four nucleon systems could be investigated. Primakoff [47] has stressed the desirability of measuring the neutron spectra in the low energy neutrino limit for deuterium and  $^3\text{He}$ , citing that such an emission geometry is an effective probe of the contribution from meson exchange currents. By measuring the neutron spectra for  $^4\text{He}$ , an effect due to closed nucleon shells on energetic particle emission may be observed. This work would be useful in discriminating various theories of particle emission after  $\mu^-$  capture in heavier

nuclei.

## 5.1 An Improved Technique for Deuterium

The fact that the results of the present measurement do not lead to firm conclusions regarding energetic neutron emission has motivated the desire to repeat the experiment. The major deficiency of the present measurement was the poor statistics, which was a reflection of the high background levels and low counting rates. The focus of the new proposal was techniques to reduce the prohibitive background and to increase the neutron detection efficiencies. The following are among the proposed improvements:

1. implementation of liquid scintillators for the time-zero counters; this would enable  $n - \gamma$  discrimination by means of pulse shape discrimination (PSD);
2. tuning the channel for a smaller momentum bite and lower  $\mu^-$  momentum; simulation of the detection efficiency by MONTY has shown that the efficiency is sensitive to the assumed stopping profile. By lowering momentum, the beam may be more effectively focussed on the central half of the target, where simulations predict the largest number of coincidences would result;
3. an improved  $\mu^-$  telescope and additional veto counters: the telescope elements would have individual TDC's for better analysis of pile-up events; additional veto counters are to be placed between the beam line aperture and time-zero counters to veto events from charged particles not detected by the telescope system;
4. addition of a 1/16" thick scintillators in front of each Far counter in order to improve the charged particle veto efficiency;

5. improved shielding near the beam line aperture and additional concrete blocks between the main beam line and Far counters. It is believed that a component of the background is due to particles produced in the target area T2.
6. removal of the hardwired back to back coincidence pattern for all data acquisition; this would allow greater flexibility in the off-line analysis. More important is that the efficiency of the TOF system would be increased significantly by relaxing the angular requirement to  $26^\circ$ . This effect is due to the finite target volume and the required coincidence pattern for the neutron counter arrays.

### 5.1.1 Pulse Shape Discrimination

The primary source of background in the present measurement was attributed to  $\gamma$ -rays. This is in agreement with the results of a post-experiment test of the nature of the neutral particle background in the M20A area. A liquid scintillator with PSD capabilities was placed at the approximate position of the Far counters; the measurement showed that neutron background was approximately 2% of the  $\gamma$  background.

Certain types of organic scintillators have the property that the pulse due to a massive ionizing particle, *i.e.* a proton, has a different shape from that of an electron. By measuring the time taken from the start of the pulse to the point where the integrated signal has reached some large fraction of the total signal, the nature of the particle producing the signal may be inferred. A photon, which is detected via Compton scattered electrons or pair production, will produce a integrated pulse with a fast rise-time whereas a neutron will give rise to a "slower" pulse.<sup>1</sup> The above technique is known as the zero-crossover method of PSD as the integration

---

<sup>1</sup>The difference in the primary pulses is that an electron will produce pulse with a relatively larger "prompt" component and smaller "delayed" component where the converse applies to a proton or heavier charged particle.

time corresponds to the zero-crossover time of the doubly differentiated primary pulse.

In the proposed new experiment the plastic Near counters are to be replaced with BC-501<sup>2</sup> liquid organic scintillators. The PSD modules to be employed are those developed by Caffrey *et al.* [48] in conjunction with  $\mu^-$  catalyzed fusion studies. The system is based on the cross-over timing technique and has been optimized to provide good  $n - \gamma$  discrimination without sacrificing deadtime. The deadtime is 150 ns or less while conventional pulse shape discriminators have times of 300 to 1000 ns. The availability of PSD would allow lowering of the detector threshold to increase the efficiency while simultaneously reducing the background; a conservative estimate puts the background reduction at a factor of 4 and the increase in efficiency at 2.<sup>3</sup>

### 5.1.2 Neutron Detection System

In the first run of the experiment, there was a hard wired logic requirement of a back-to-back firing pattern for the first 60% of data acquisition; only events within  $16^\circ$  of a pure back-to-back geometry were accepted in the Master gate. This requirement limited the possible analysis techniques for the data: an estimate of the background in the kinematic region of interest may be obtained by considering the spectrum produced by requiring  $\theta > 16^\circ$ . Above this limit, neutrons of energy greater than 23 Mev are kinematically forbidden<sup>4</sup>. Lee *et al.* [49] have performed this analysis and have shown that background in the 35 to 50 Mev region is consistent with zero. Unfortunately, this mode of analysis was available only for the data without the back-to-back requirement.

A Monte Carlo simulation to explore the effect of easing the angular

---

<sup>2</sup>Bicron Co.

<sup>3</sup>Private communication with Y.K. Lee

<sup>4</sup>Neglecting the finite target effect.

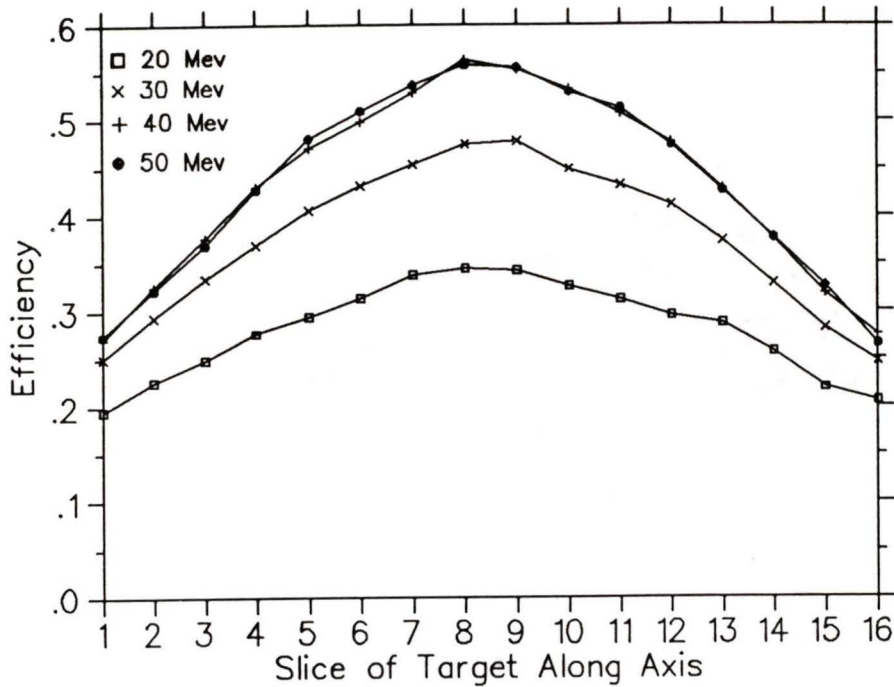


Figure 5.1: Coincidence efficiency for  $\Delta\theta < 26^\circ$ . Compare with Fig. 4.7.

requirement to  $\theta \leq 26^\circ$  shows pronounced enhancements of coincidence efficiency. The only difference between the simulated results shown in Fig. 5.1 and 4.7 is the addition of new pairs of counters in the neutron counter latch pattern in Fig. 5.1. Based on this analysis, the proposed changes in the allowed latch pattern for the off-line analysis are:

- time-zero counters 1,2 in coincidence with Far counters 1-4,  $\Delta\theta \leq 21^\circ$  ;
- time-zero counters 3,4 in coincidence with Far counters 2-7,  $\Delta\theta \leq 26^\circ$  ;
- time-zero counters 5,6 in coincidence with Far counters 5,10  $\Delta\theta \leq 26^\circ$  ;
- time-zero counters 7,8 in coincidence with Far counters 9-12  $\Delta\theta \leq 21^\circ$  .

The proposed arrangement is shown in Fig. 5.2.

This analysis was performed on the data without the hard wired back-to-back bias using the new, ( $\Delta\theta < 26^\circ$ ), coincidence requirement

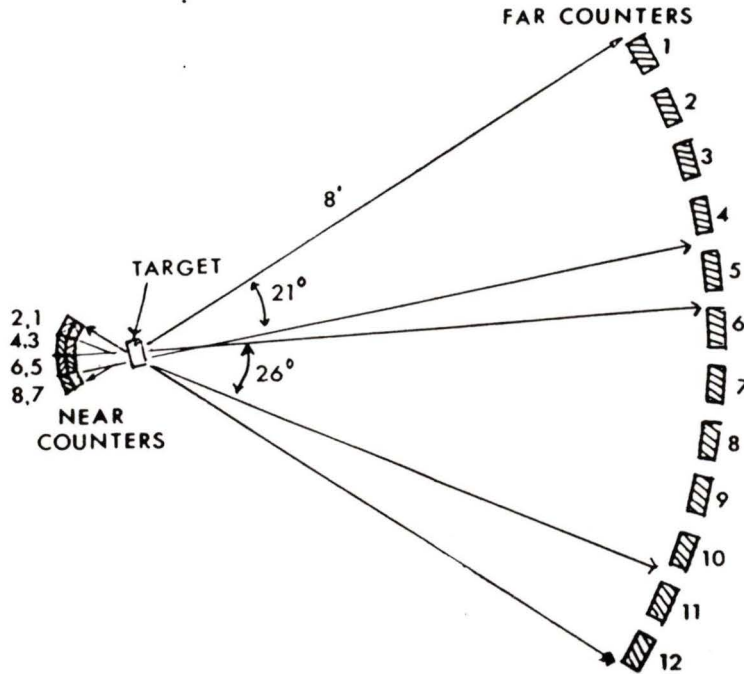


Figure 5.2: Proposed counter arrangement showing the angular acceptance for new latch pattern.

and the original  $16^\circ$  requirement for identical threshold values. The results, presented in Figs. 5.3 and 5.4 show the time-of-flight spectra after a background subtraction based on the 13 to 22 ns interval. The spectrum for the relaxed latch pattern shows a 136% increase in the number of counts in the 25 to 55 Mev range (22 to 33 ns in the figures). The background exhibited a 92% increase, contrary to the expected 50% increase. The 50% increase would correspond to the increase in “effective solid angle” of the detection system obtained by relaxing the latch pattern. Part of the unexpected background increase can be attributed to geometric considerations and possible background anisotropy. The thresholds used for the comparison were 5.6 Mev<sub>e.e.</sub> for the Far and 3.6 Mev<sub>e.e.</sub> for the Near counters, respectively. From inspection of the TOF vs. amplitude scatterplots, it is evident that the threshold cuts have not been optimized for the new latch pattern. The most significant result though, is the increase in signal to background ratio (S/B) in the 25-52 Mev range; the ratio for the new latch

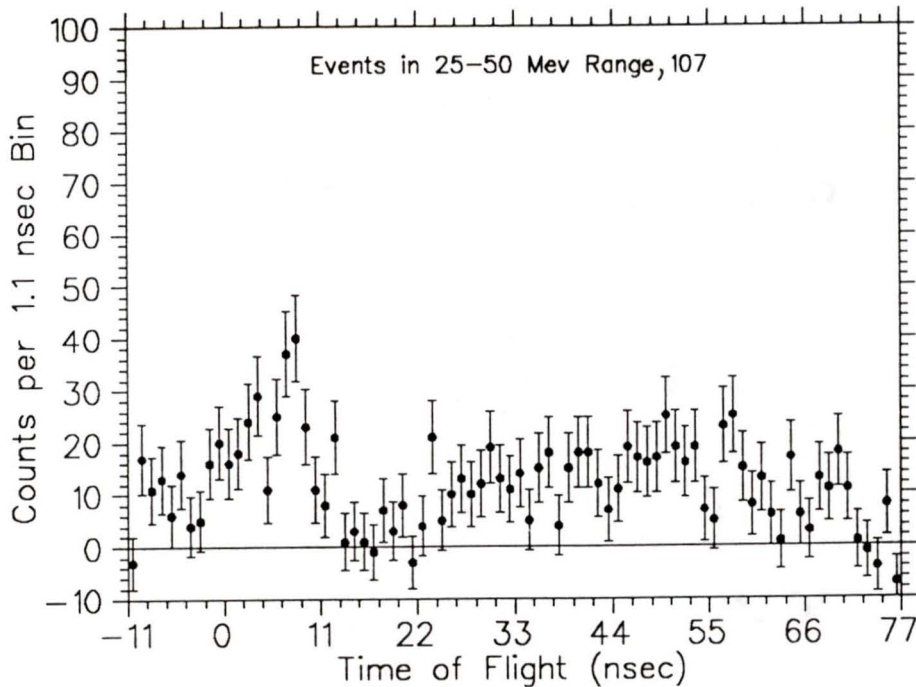


Figure 5.3: Time-of-flight spectrum for  $\Delta\theta < 16^\circ$ . The 22 to 33 ns interval has 368 counts with a background of 261.

pattern S/B to that of the old arrangement is  $1.229 \pm .009$ . For the proposed rerun, with the improvements to be implemented, the effect of the increase in background would be offset by the availability of PSD. For the conservative estimate of a factor 4 reduction in the background, the net background would be 1/2 the level of the present measurement with a conservative estimate of 1.5 times the number of events, not taking into account the increase in efficiency due to the lower thresholds.

By varying the allowed latch pattern in the software analysis and fitting the Monte Carlo simulation of the change in the spectrum to the observed change, the muon stopping distribution may be indirectly measured by finding the assumed distribution that yields the best fit. For the present measurement, the uncertainty in the stopping distribution was the greatest source of systematic error in calculating the final spectrum. This technique of determining the distribution with the present data was not uti-

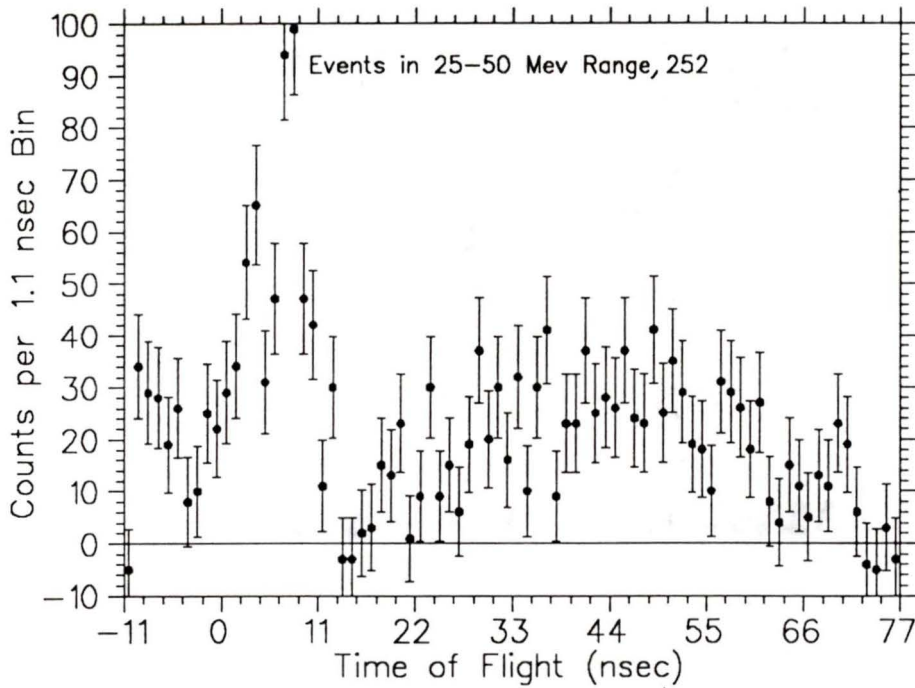
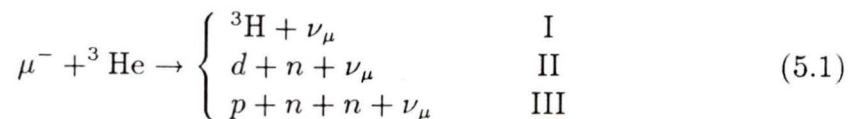


Figure 5.4: Time-of-flight spectrum for  $\Delta\theta < 26^\circ$ . The 22 to 33 ns interval has 752 counts with a background of 500.

lized because of the poor statistics; the uncertainty in the bin counts was comparable to the effect of different stopping distributions. If the statistics were improved, this might be a viable method of determining the stopping distribution.

## 5.2 Measurement of the Neutron Spectra for ${}^3\text{He}$

Negative muon capture on  ${}^3\text{He}$  can proceed along 3 basic channels.



The previous work concerning muon capture on  ${}^3\text{He}$  has focussed on the total capture rate and the partial rate,  $\Lambda_I$ , for reaction I. The triton final

state channel is the closest nuclear analogue to capture on protium. The partial capture rate has been measured [50,51,52] and the accepted world average is  $1529 \pm 37$  [1]. This value is in agreement with theoretical predictions based on the elementary particle method [53] and impulse approximation [54]. The theoretical predictions are consistently lower though not in disagreement. Clay *et al.* [50] and Auerbach *et al.* [51] both used high pressure  $^3\text{He}$  gas targets. Experimental results were obtained by observation of the scintillation produced by the recoiling triton, which has a unique energy of 1.89 Mev, and by comparison with the total number of stopped muons.

The total capture rate has also been measured [51,52] and a value of the “breakup” reaction rates, reactions II and III, can be inferred, though not individually:

$$\Lambda_{\text{II+III}} = \begin{cases} 660 \pm 160 \text{ s}^{-1} & \text{ref. [50]} \\ 665^{+170}_{-430} \text{ s}^{-1} & \text{ref. [51]} \end{cases} \quad (5.2)$$

Calculations of the breakup capture rates have been performed [55]. The results of these calculations differ widely, up to 35%, and the discrepancies have been attributed to the somewhat crude approximations employed [20]. Phillips *et al.*[20] in a recent and more refined treatment have calculated the breakup rates to be  $\Lambda_{\text{II}} = 414 \text{ s}^{-1}$  and  $\Lambda_{\text{III}} = 209 \text{ s}^{-1}$ . Their error is predicted to be no more than 10 % and is due to the neglect of MEC corrections and relativistic effects. The total neutron rate has been measured; the first measurement of the  $\mu^-$  capture rate on deuterium, performed by Wang *et al.*[15], was under conditions where the production of muonic  $^3\text{He}$  was large.<sup>5</sup> A result of  $1200 \pm 170 \text{ s}^{-1}$  was published for the neutron rate corresponding to  $\Lambda_{\text{II}} + 2\Lambda_{\text{III}}$ . The result differs by two standard deviations from the prediction of Phillips *et al.*

---

<sup>5</sup>See Chapter 2, Section 2.1.1

A measurement of the neutron spectra for  $^3\text{He}$  would not suffer from some of the problems associated with the deuterium measurement. The  $^3\text{He}$  measurement would be “cleaner”: meso-molecular processes leading to fusion would be absent; a muonic helium atom possesses a net electric charge, which inhibits the muon transfer process to heavier nuclei and the time-zero signal for the time-of-flight measurement may be directly extracted from the target. Furthermore, for reasons to be outlined, the anticipated event rate would be substantially higher than for deuterium.

The overall capture rate is much greater than that of deuterium; although the primary channel (I) does not produce neutrons, the rate for the second channel (II) is comparable to that of deuterium. A possible source of neutron background is the third channel (III); however, from phase space considerations, the neutron background in the 40 to 70 Mev range from this reaction would be essentially zero. This is the kinematic region for channel II where MEC effects could be detected.

### 5.2.1 Experimental Technique for $^3\text{He}$

The experimental technique to measure the neutron spectrum from capture on  $^3\text{He}$  is similar to that of deuterium. A fundamental difference, though, is the employment of the liquid  $^3\text{He}$  target as the scintillant for the time-zero signal. An additional improvement would be the implementation of liquid scintillators for the Far counter neutron array which would allow  $n - \gamma$  discrimination as well as reasonably fast timing resolution. The proposed arrangement is to have an array of twelve neutron counters ( $25 \times 6 \times 3 \text{ cm}^3$ ) placed 2.44 m (8') from the target in order to provide good time-of-flight resolution. The telescope design and logic would be similar; however the required signal to indicate a stopped muon would include a signal from the  $^3\text{He}$  scintillant.

The liquid scintillators would enable investigation of a greater region

of the neutron spectrum. The of  $n - \gamma$  discrimination afforded by the liquid scintillators coupled with the absence of the low energy neutron background from fusion implies that the thresholds for the detectors may be set at lower levels in the off-line analysis than those for the present measurement. This would substantially increase the neutron detection efficiencies. The availability of a direct time-zero signal would eliminate the finite target effect on the coincidence efficiency. The detection efficiency for the helium scintillation light producing the time-zero signal is expected to be approximately 0.8 [46], which is about 8 times greater than the detection efficiency for the second neutron required for the deuterium experiment.

The experiment would be almost kinematically complete,<sup>6</sup> enabling partial discrimination between the two capture channels leading to neutrons in the final state. A second array of neutron detectors would be used to detect the secondary neutrons from channel III. The detectors would be placed a distance that provides reasonable time-of-flight resolution compatible with a high solid angle efficiency. The liquid  $^3\text{He}$  target will allow a energy measurement of the particle producing the time-zero signal within 10%. This coupled with the time-of-flight measurement for the detected neutron would allow partial discrimination of channel III events for the case where the second neutron is not detected. The technique is, however, limited by the wall effect on the energy determination of the charged particle inducing the time-zero signal. An energetic particle, depending on the capture point, might not liberate its full energy to the scintillator before exiting the target. This effect may be corrected for by a Monte Carlo simulation taking into account the muon stopping distribution, the energy and detection position of the neutron.

---

<sup>6</sup>The energies of two of the final state particles will be measured.

### Liquid Helium Target

By using the known scintillation properties of helium [56], a time-zero signal for the time-of-flight measurement may be extracted by observation of the charged particle produced at capture. The advantage of this is obvious: there is no kinematic effect on the energy resolution as in the case where the time-zero signal is produced by a correlated massive particle detected at some distance from the interaction point. The timing resolution for a liquid  $^3\text{He}$  neutron spectrometer similar to the proposed target has been measured and a value of 1.2 ns FWHM has been published [57]. The relationship of the pulse height to energy deposition for helium is linear. The monoenergetic triton final state from the primary capture channel would provide an excellent calibration point at 1.89 Mev for the pulse height spectrum of the  $^3\text{He}$  scintillator. A liquid helium target also has the advantage of self-purification, as any gaseous impurities would “freeze” out in the liquification process.

The target has yet to be designed; a primary consideration is that the target must be relatively thick to minimize the wall effect. Ideally, the dimensions of the target in the plane of the neutron counters should be such that the minimum distance from the center of the target to the walls should not be less than 40 mm. This corresponds to the range of 27 Mev deuterons and 17 Mev protons in liquid  $^3\text{He}$ , respectively. The target dimensions in the beamline direction should be such as to provide a relatively thick stop for the incident muons. From these considerations, a suitable design would be a right cylinder of 80 mm diameter by 50 mm height. The window for observing the scintillation would be the bottom endcap. The active volume of  $^3\text{He}$  would be 250 cm<sup>3</sup>.

The scintillation spectrum lies in the ultraviolet regime; this necessitates employment of a wavelength shifter to coat the inner walls and window. van Staa *et al.* [57] have investigated the energy resolution and

efficiency for various wavelength shifters; they note that diphenylstilbene (DPS) is the most favourable choice if the photomultiplier tube has a bialkali cathode. The window must be made of a transparent yet good heat insulating material; previously constructed liquid helium scintillators have employed mylar, quartz or sapphire windows.

# Chapter 6

## Conclusion

The results of TRIUMF experiment 297 have shown that it is possible to measure the energetic component of the neutron spectra to sufficient accuracy to detect evidence of the predicted enhancement due to meson exchange currents. The dominance of the systematic error and the poor statistics, though, do not allow a firm interpretation of the data. In order to conclude that there is definite structure in the high energy component of the neutron spectrum, the experiment would have to be repeated. The proposed improvements, as outlined in Chapter 5, would allow such a conclusion. The counting rate in the region of interest is small; the capture rate for deuterium is three orders of magnitude smaller than the muon decay rate and the cross section in the region of interest is only 3% of the total capture rate; as well, the detection efficiency for the present measurement for 45 Mev neutrons was only  $6.1 \times 10^{-5}$  for the detector thresholds employed. The fact that there is an indication of an enhancement is promising. A new experiment with a longer running time, hence, improved statistics, would clearly show conclusive results.

The present uncertainty in the mechanism responsible for energetic particle emission following nuclear muon capture requires clarification. Studies of neutron spectra from capture on heavy nuclei, though experimentally more accessible, suffer from model dependent interpretations due to the inherent complexity of many-nucleon systems. Investigations of the neutron

spectra for light nuclei are experimentally more difficult, but can lead to sound interpretations because of the far better understanding of nuclear processes involved.

Performing experiments on heavier nuclei to test the hypothesis that meson exchange corrections are responsible for energetic particle emission does have limitations. The hypothesis is optimally tested for very light nuclei, where excited bound nuclear states are absent. In nuclei with  $A \leq 4$ , a “global” measurement of the spectrum is possible, in capture on heavier nuclei there are nuclear transitions in the final state implying that the measured spectrum would be due to a sum over these states. Such an effect would “wash out” the MEC induced enhancement unless the spectra from individual final states could be differentiated. More important, though, is that for deuterium and  $^3\text{He}$ , there is the absence of other nuclear phenomena that could explain an enhancement in the high energy neutron spectrum. Such a process would have other effects that would have been hitherto observed. It is important to repeat the experiment for deuterium and extend the technique to helium as a means of determining the extent of meson exchange current effects.

# Bibliography

- [1] N.C. Mukhopadhyay, *Nuclear Muon Capture*, Physics Reports 30C (1977) 1
- [2] J.A. Wheeler, Rev. Mod. Phys. 21 (1949) 133
- [3] E.K. MacIntyre, T.J. Hallman, K.S. Kang, Y.K. Lee, L. Mandansky, G.R. Mason, Phys. Lett. 137B (1984) 339
- [4] J. Bernabéu, T.E.C. Ericson and C. Jarlskog, Phys. Lett. 69B (1977) 161
- [5] B. Goulard, B. Lorazo and H. Primakoff, Phys. Rev. C26 (1982) 1237
- [6] G. Bardin, J. Duclos, J. Martino, A. Bertin, M. Capponi, M. Piccinini and A. Vitale, Nucl. Phys A453 (1986) 591
- [7] TRIUMF Research Proposal Expt. no. 297, Spokesman Prof. Y.K. Lee
- [8] F. Dautry, M. Rho and D.O. Riska, Nucl. Phys. A264 (1976) 507
- [9] M. Sontona and E. Truhlík, Phys. Lett. 43B (1973) 362 ; Nucl. Phys. A229 (1974) 471
- [10] D.O. Riska and G.E. Brown, Phys. Lett. 38B (1972) 193  
J. Hockert *et al.*, Nucl. Phys. A217 (1973) 14
- [11] E. Ivanov and E. Truhlík, Nucl. Phys. A316 (1979) 451

- [12] G.E. Dogotar, R.A. Eramzhyan and E. Truhlík, Nucl. Phys. A326 (1979) 225
- [13] S.L. Mintz, Phys. Rev. D8 (1973) 2946;  
Phys. Rev. C22 (1980) 2507; Phys. Rev. C28 (1983) 556
- [14] H. Primakoff, Rev. Mod. Phys. 31 (1959) 802  
A. Fujii and H. Primakoff, Nuovo Cimento 12 (1959) 327
- [15] I.T. Wang, E.W. Anderson, E.J. Bleser, L.M. Ledermen, S.L. Meyer,  
J.L. Rosen and J.E. Rothberg, Phys. Rev. B139 (1965) 1528
- [16] A. Bertin, A. Vitale, A. Placci and E. Zavattini, Phys. Rev. D8 (1973)  
3774
- [17] P. Kammel, W.H. Breunlich, M. Cargnelli, H.G. Mahler, J. Zmeskal,  
W.H. Bertl and C. Petitjean, Phys. Rev. C28 (1983) 2611
- [18] D.V Balin et al., LINP preprint (1981) 715, Gatchina Group, Third  
Int. Conf. on Emerging Nuclear Energy Systems, Helsinki (1983)
- [19] W.H. Breunlich, Nucl. Phys. A353 (1981) 201c
- [20] A.C. Phillips, F. Roig and J. Ros, Nucl. Phys A237 (1975) 493
- [21] E. Fermi, Ric. Sci. 2 (1933) Pt. 12 ; Z. Phys. 88 (1934) 161
- [22] J.J. Sakurai, *Currents and Mesons* (Chicago University Press, Chicago  
and London, 1969)
- [23] M. Gell-Man, Phys. Rev. 125 (1962) 1067  
N. Cabbibo, Phys. Rev. Lett. 10 (1963) 53
- [24] T.D. Lee and C.N. Yang, Phys. Rev. 104 (1956) 254 ; Phys. Rev. 105  
(1957) 1671

- [25] C.S. Wu, E. Ambler, R.W. Hayward, D.D. Hoppes and R.P. Hudson, Phys. Rev. 105 (1957) 1413
- [26] R.P. Feynman and M. Gell-Man, Phys. Rev. 109 (1958) 193
- [27] Ya. Zel'dovich and S.S. Gerstien, Sov. Phys. JETP 2 (1957) 576
- [28] S. Weinberg, Phys. Rev. 112 (1958) 1375
- [29] *Review of Particle Properties*, Phys. Lett. 170B (1986)
- [30] S.L. Adler, Phys. Rev. Lett. 14 (1965) 1051
- [31] W.I. Weisberger, Phys. Rev. Lett. 14 (1965) 1047
- [32] J.D. Walecka (Muon Physics, Vol. II, C.S. Wu and V. Hughes (eds.), Academic Press, New York, London, 1975)
- [33] M.L. Goldberger and S.B. Treiman, Phys. Rev. 111 (1958) 354
- [34] I.T. Wang, Phys. Rev. 139 (1965) B1539
- [35] P. Pascual, R. Tarrah and F. Virdal, Nuovo Cimento 12A (1972) 241
- [36] R. V. Reid, Jr., Ann. of Phys. 50 (1968) 411
- [37] A.J. Caffrey *et al.*, Bull. Am. Phys. Soc. 32 (1987) 1031
- [38] MOLLI: Multi OffLine Interactive analysis, TRIUMF reference manual, A. Bennett, C. Kost, 1985
- [39] FIOWA: Fast Input Output With Analysis, TRIUMF reference manual, A. Hayes, A. Bennett, 1981
- [40] G.L. Knoll, *Radiation Detection and Measurement* (John Wiley & Sons, New York and Toronto, 1979)

- [41] T.J. Gooding and N.G. Pugh, Nucl. Instr. and Meth. 7 (1960) 189
- [42] T. Suzuki, J.P. Roalsvig and D.F. Measday, submitted to Phys. Rev. C
- [43] N.R. Stanton, preprint Ohio State University COO-1545-92 (1971);  
R.A. Cecil, B.D. Anderson and R. Madey, Nucl. Instr. and Meth. 161  
(1979) 439
- [44] M. Elfield *et al.*, Nucl. Instr. and Meth. 100 (1972) 237
- [45] TRIUMF Research Proposal Expt. no. 465, MUDEUT Group
- [46] TRIUMF Research Proposal Expt. no. 451, NEMUCALIHE Group
- [47] H. Primakoff, A.I.P. Conference Proceedings number 37, *Weak Interaction Physics-1977*, Indiana University (D.B Lichtenberg, Editor)
- [48] A.J. Caffrey *et al.*, IEEE Nucl. Sci. Symposium, San Francisco, CA. (1987)
- [49] Y.K. Lee *et al.* Phys. Lett., B188 (1987) 34
- [50] D.R. Clay, J.W. Keuffel, R.L. Wagner and R.M. Edelstien, Phys. Rev. 140 (1965) B586
- [51] L.B. Auerbach, R.J. Easterling, R.E. Hill, D.A. Jenkins J.T. Lach and H.H. Lipman, Phys. Rev. 138 (1965) B127
- [52] I. V. Falmokin, O.A. Zaimidoroga, M.M. Kulyukin, B. Pontecorvo, R.M. Sulyaev, A.I. Filippov, V.M. Tsupko-Sitnikov and Yu. A. Scherbakov, Phys. Lett. 3 (1963) 229
- [53] A. Fujii and Y. Yamaguichi, Progr. Theoret. Phys. 31 (1964) 107  
W. Drechsler and B. Stech, Z. Phys. 178 (1964) 1  
A. Santisteban and R. Pascual, Nucl. Phys. A260 (1976) 392

- [54] E.M. Peterson, Phys. Rev. 167 (1968) 971  
E. Guancial and D. Lin, Nuovo Cim. A67 (1970) 538
- [55] A.F. Yano, Phys. Rev. Lett. 12 (1964) 110  
P. Pascual and R. Pascual, Nuovo Cim. 48 (1967) A963  
R. Pascual, Nucl. Phys. B3 (1967) 561  
I-T. Wang, Phys. Rev. 139 (1965) B1544
- [56] E.H. Thorndike and W.T. Shaler, Rev. Sci. Instr. 30 (1959) 839  
J.E. Simmons and R.B. Perkins, Rev. Sci. Instr. 32 (1961) 1173
- [57] R. van Staa, J. Reher and B. Zeitnitz, Nucl. Instr. and Meth. 136  
(1976) 241

## Vita

Surname: **Turcot**

Given Names: **André Spence**

Place of Birth:

**Halifax, Nova Scotia**

Date of Birth:

**September 23, 1962**

Educational Institutions Attended:

**Saint Mary's University, N.S.**

**1978 to 1982**

**Concordia University, P.Q.**

**1982 to 1985**

**University of Victoria, B.C.**

**1985 to 1987**

Degrees Awarded:

**B.Sc. 1985**

**Concordia University**

Honors and Awards:

**St. Mary's U. Achievement Scholarship**


**1979**

# Partial Copyright License

I hereby grant the right to lend my thesis (the title of which is shown below) to users of the University of Victoria Library, and to make single copies only for such users, or in response to a request from the library of any other university or similar institution, on its behalf or for one of its users. I further agree that permission for extensive copying of this thesis for scholarly purposes may be granted by me or a member of the university designated by me. It is understood that copying or publication of this thesis for financial gain shall not be allowed without my written permission.

Title of Thesis:

**MEASUREMENT OF NEUTRON SPECTRA  
FOLLOWING STOPPED MUON CAPTURE  
ON LIQUID DEUTERIUM**

  
Author André Spence Turcot

August 28, 1987